On the influence of magnetic mineralogy in the tectonic interpretation of Anisotropy of Magnetic Susceptibility in cataclastic fault zones

Teresa Román-Berdiel[1], Antonio M. Casas-Sainz[1], Belén Oliva-Urcia[2], Pablo Calvín[3], Juan José Villalaín[3]

[1]*Departamento de Ciencias de la Tierra, Geotransfer Research Group, Instituto de Investigación en Ciencias Ambientales (IUCA), Universidad de Zaragoza, Pedro Cerbuna 12, 50009 Zaragoza, Spain. E-mail: mtdjrb@unizar.es*

[2]*Departamento de Geología y Geoquímica, Universidad Autónoma de Madrid, Spain*

[3]*Laboratorio de Paleomagnetismo, Departamento de Física, Universidad de Burgos, Spain*

Abbreviated title: *Influence of magnetic mineralogy in AMS of fault zones*

SUMMARY

Of the several factors involved in the development of magnetic fabrics in fault zones at shallow crustal levels, lithology and deformation intensity have probably the most important consequences for the reconstruction of their kinematic history. The basement-involved Cenozoic thrusts in the Demanda Massif (N Spain) provide the opportunity for testing the applicability of Anisotropy of Magnetic Susceptibility (AMS) to the study of deformation in cataclastic fault rocks belonging to shallow fault zones. The Rastraculos thrust is a relatively minor basement thrust (dip-slip movement of 2 km defined from cross-sections and geological maps) of Cenozoic age. This thrust contains a re-activated fault zone involving different rock types both belonging to its hangingwall (Paleozoic) and its footwall (Triassic sandstones and dolostones and Jurassic limestones). AMS results show magnetic foliations parallel or slightly oblique to the fault zone, and both transport-parallel (projected onto the foliation plane) and transport-perpendicular (parallel to the observed intersection lineation) magnetic lineations. The two types of strain/magnetic fabric

relationships can be related to deformational and mineralogical features inferred from the direct analysis of thin and polished sections under the microscope and the naked eye, respectively. Analysis of fault rocks in the Rastraculos fault zone indicates that in cataclasites, magnetic fabrics are particularly dependent on lithology and hence magnetic mineralogy. The results obtained prove the usefulness of AMS in fault zones where kinematic indicators are scarce and also give clues on the number of samples necessary to define magnetic susceptibility axes, depending on grain size, ellipsoid shapes and magnetic mineralogy.

Keywords: Magnetic fabrics and anisotropy; Fractures, faults, and high strain deformation zones; Microstructures; Intra-plate processes; Continental tectonics: compressional; Europe.

1 INTRODUCTION

Magnetic fabrics in fault zones depend on the particular conditions of each fault (also considering its type, reverse, normal or strike-slip) and the features of the protolith of the fault rock. These conditions include strain intensity, magnetic mineralogy, grain size, and lithology of fault rocks (Parés & Van der Pluijm 2002a). The relative weight of each of these factors can condition the relationships between the magnetic ellipsoid, the petrofabric and their orientation with respect to other kinematic indicators, such as S-C structures in fault gouges or slickenside striations developed on foliation or shear surfaces. Since Anisotropy of Magnetic Susceptibility (AMS) has begun to be systematically used as an indicator of the kinematics in fault zones (Solum & Van der Pluijm 2009; Mertainen & Karell 2012; Levi *et al.* 2014; Moreno *et al.* 2014; Pomella 2014; Braun *et al.* 2015; Keskineva *et al.* 2016; Casas *et al.* 2017), checking its reliability and determining the factors influencing its results is of primary importance before considering its wholesale

application to each particular fault zone. Although the relationships between the petrofabric and the magnetic fabric under homogeneous strain at depth are clearly defined and have been interpreted to depend on the intensity of deformation (Parés & Van der Pluijm 2002a), at shallow depths interpretation of fault rocks is more complicated. Casas *et al.* (2017) showed that magnetic mineralogy, intensity of deformation and the type of structures (including macroscopic S-C structures and grain deformation and orientation) are determinant in the definition of the relationship between the magnetic ellipsoid and the petrofabric. Therefore, an effort must be done in order to define structural elements separating homogeneous domains within fault zones.

In this work we explore, from a thorough study that comprises more than one thousand samples, a relatively small fault zone with a simple kinematic history. From this study, we define the influence of lithology (shales, limestones and sandstones belonging to different stratigraphic units), intensity of deformation (by comparing magnetic fabrics with petrofabric of sheared rocks) and magnetic mineralogy, both ferro- and para-magnetic (defined by hematite and phyllosilicates) in the development of the magnetic fabric of fault cataclasites. Finally, from comparison with structural markers both at the macro- (geological cross-sections and maps, cut-off relationships…), meso- (mainly, outcrop observation of structures, somewhat limited because of the exposure conditions) and micro-scale (S-C structures, foliation and lineation in polished and thin sections under the microscope), we define the meaning and limits of application of AMS in this type of fault rocks.

The Rastraculos thrust shows an overall E-W orientation, contrasting with other areas of the Iberian Chain in which NW-SE direction is the dominant trend (Gil-Serrano *et al.* 1977; Cámara & Durantez 1978; Fig. 1A). In this case, frontal thrusting is the *a priori* most

significant process during the Cenozoic N-S compression (see e.g. Guimerà & Alvaro 1990; Casas *et al.* 2017). The Rastraculos thrust probably formed because of the re-activation of a Late-Variscan fault, what explains its relatively thick (tens of meters) fault zone, including breccia and fault gouge. This circumstance has allowed to test AMS in different types of rocks, showing different deformation degree, and resulting from the deformation of different stratigraphic units each having distinct magnetic mineralogy. Nevertheless, since the analyzed rocks only include Triassic and Jurassic units, the recorded deformational history is relatively simple and corresponds uniquely to the Cenozoic compressional period. The techniques applied in this work include routinely used magnetic methods to determine magnetic mineralogy and AMS parameters, and structural analysis, at the outcrop scale, in cut and polished sections observed with the naked eye, and in thin section under the microscope. These techniques are aimed to obtain a reliable picture of the relationships between magnetic fabrics and geological structures in shallow-depth cataclasites.

2 GEOLOGICAL SETTING

The Demanda Massif is one of the most prominent Paleozoic outcrops outside the Iberian Variscan Massif, showing an elliptical shape in map view. Its present structure results from northwards thrusting of Paleozoic rocks over the syn-tectonic units of the Rioja Trough (Ebro Basin) during the Cenozoic (Guimerà & Alvaro 1990; Fig. 1A). Both Variscan and Alpine structures can be recognized in the Demanda Massif: Variscan structures consist mainly in north-verging, kilometric-scale folds (reaching wavelengths of 8 km and amplitudes of 3 km in some cases) and low-angle thrusts (Colchen 1974). Late-Variscan faults limiting Stephanian-Permian basins and cutting the Variscan structures show NW-SE to E-W direction and subvertical dips, although syn-tectonic deposits associated with these

faults have been only identified in the westernmost part of the massif (Colchen 1974).

The Paleozoic outcrop of the Demanda Massif is divided into two unequal parts by the Villavelayo syncline (Casas-Sainz & Gil-Imaz 1998), a plurikilometric E-W structure that can be followed more than 30 km along trend. Its core is occupied by Triassic to Cretaceous calcareous and terrigenous deposits (Fig. 1) having a cumulate preserved thickness of 2 about km. The western end of the Villavelayo syncline abuts against the main Late-Variscan fault in the area, and towards the East it drowns below the thick Lower Cretaceous deposits of the Cameros Massif (Soto *et al.* 2008; Fig. 1). South of the Villavelayo syncline, Variscan folds show a NW-SE trend, slightly oblique to the main Variscan E-W trend in the northern sector of the Demanda Massif (Yenes *et al.* 1990).

The Paleozoic series of the Demanda Massif consists mainly of Cambrian sandstones and shales up to 5000 m thick overlying Precambrian shales. Only in the westernmost sector of the Demanda Massif and also within the core of the Najerilla syncline (Fig. 1A) do younger Paleozoic, pre-Variscan sediments (mainly Ordovician sandstones and shales) crop out. Finally, as previously mentioned, post-Variscan Paleozoic sediments (mainly conglomerates) appear associated to the Late-Variscan faults (Colchen 1974). In the study area, Variscan folds are parallel to the E-W trend of the Cenozoic structure in the hanging wall of the Rastraculos thrust. However, in its footwall, some kilometers far from the trace of the thrust, strongly oblique NW-SE anticlines are the main structures of Variscan origin (Colchen 1974). These folds are probably cut at depth by the alpine structures, and are unconformably covered by the Lower Triassic or, alternatively, the Lower Jurassic (Liesa-Carrera & Casas-Sainz 1994). Regional, axial plane foliation associated to Variscan folds is only present in shaly units, and usually shows a steep dip, forming a low angle with bedding in the limbs of folds (Liesa-Carrera & Casas-Sainz 1994).

The Rastraculos thrust can be followed 18 km along strike. Its mapped trace changes from NE-SW orientation in its western sector, to E-W in its central and eastern sectors (Fig. 2A). Since it cuts through Variscan structures, the geometry of its hanging wall (Fig. 2B) can only be reconstructed from the attitude of Mesozoic beds (Triassic and Jurassic) that show an ENE-WSW strike and intermediate southward dips in most of the area (Fig. 2D and E). In the footwall of the Rastraculos thrust the Triassic and Jurassic beds also show a southward dip. The net slip in the central part of the thrust can be estimated in 2 km, gradually diminishing toward both ends (Fig. 2A). Our study was focused on the easternmost segment of the thrust, where it shows a 20 m thick fault zone, and probably results from the partial re-activation of a Late-Variscan, steeply dipping fault having NW-SE or WNW-ESE orientation (Fig. 2B). This hypothesis is supported by the fact that the Paleozoic rocks cropping out in the footwall and the hangingwall in close areas show different age and facies. The fault zone consists of strongly weathered fault gouge and breccia, resulting from the cataclasis of red beds (Lower Triassic, Buntsandstein facies), dolostones (Middle Triassic, Muschelkalk facies), limestones (mainly of Jurassic age), and Paleozoic (Cambrian) shales. Because of outcrop conditions, and with the aim of simplifying interpretations, sampling only involved the fault rocks resulting from cataclasis of the Mesozoic units, whose deformational history is exclusively linked to the Cenozoic movements of the Rastraculos thrust.

3 METHODOLOGY

As previously mentioned, sampling was done covering the area where fault rocks are more developed, i.e. the eastern half of the mapped trace of the Rastraculos thrust (Fig. 2A), where gullies and badlands, that are surrounded by a thick vegetation cover, allow for the exposure of the fault rocks. Exposures are therefore erosional scars in the middle of steeps

slopes covered with vegetation (Fig. 2D, Fig. 3A, B).

Three sections were sampled (RC1, RC2-3-4, RC5-6) trying, when possible, to cut transects of a few meters across the fault zone in order to detect heterogeneities both in the composition of rocks and in the deformation degree. Sampling sites are distributed 2 km along strike of the Rastraculos mapped trace, from East (site RC1) to West (site RC6). Sites RC2, RC3, and RC4 are located along a vertical profile 100 m long from the bottom of the valley (RC2) upslope (RC3 and RC4). RC5 and RC6 are close to one another (tens of meters) along a transect of the fault zone perpendicular to the Rastraculos fault trace, RC5 being closer to the thrust surface. Sampling was achieved by digging the weathered zone and taking hand samples, that were oriented in the field. In the laboratory, samples were embedded in plaster in order to accurately respect their orientation and cut to obtain both polished surfaces to observe structures at the mesoscopic scale (Fig. 3C, D, E, F, G, H) and cubic specimens of side length 2.1 cm for the AMS study, by means of a trim saw refrigerated with water. The high number of hand samples, totaling 46 (Tables 1 and 2), allows for averaging orientation errors during the process of handling and cutting.

Measurement of AMS was done in a total of 1054 standard specimens with a KLY-3S Kappabridge (Agico Inc., Czech Republic), installed at the Magnetic Fabrics Laboratory of the University of Zaragoza. These measurements provide the orientations and magnitudes of the $k_{max} \geq k_{int} \geq k_{min}$ axes of the AMS ellipsoid, and hence help to define the magnetic fabric that is characterized by the magnetic lineation (k_{max}) and the magnetic foliation (plane perpendicular to k_{min}). The shape of this ellipsoid and the degree of magnetic fabric development were defined by two parameters (Jelinek, 1981): (1) the corrected degree of anisotropy, P', that provides a first indication of rock deformation and preferred mineral orientation, and (2) the shape parameter, T, varying between $0 \geq T \geq -1$ (prolate ellipsoids)

and $0 \leq T \leq 1$ (oblate ellipsoids). The average directional and scalar values for each site were calculated using Jelinek's (1978) statistics with Anisoft 4.2 (Chadima & Jelinek 2009). Some specimens (21 in total) were also measured at low temperature (liquid nitrogen, 70K) in order to determine the contribution of the enhanced paramagnetic fabric and therefore to separate it from the total magnetic fabric (Ritcher & Van der Pluijm 1994; Lüneburg *et al.* 1999; Parés & Van der Pluijm 2002b; Martín-Hernández & Ferré 2007; Oliva-Urcia *et al.* 2010; Issachar *et al.* 2016). To define mineral carriers, temperature-susceptibility curves were obtained from eight samples with a CS-3 furnace and a CSL cryogenic apparatus connected to the KLY-3S (Hrouda *et al.* 1997; Petrovsky & Kapicka 2006). Data processing was performed with the Cureval 8.0 software (Chadima & Hrouda 2009). In addition, rock magnetic experiments related to magnetic remanence (hysteresis loops, backfield curves and magnetization thermomagnetic curves) were performed in four selected samples using a variable field translation balance MMVFTB (Magnetic Measurements), installed at the Paleomagnetic Laboratory of Burgos University.

The measurement of structural data in the outcrops is difficult, given the intensely brecciated state of the rocks and the intense weathering and debris cover in the gullies (Fig. 2D and Fig. 3A, B). Thus, in order to check the meaning of magnetic fabrics, for each hand sample or sector, at least two thin sections were cut and observed under the petrographic microscope (Figs. 4, 5). One of the sections is a vertical plane perpendicular to the magnetic foliation, and the other section is perpendicular to the magnetic foliation and contains the horizontal line. Given the orientation of the magnetic lineation in most sites (either horizontal or along the dip direction of magnetic foliation), one of the studied sections contains the magnetic lineation and the other one is always perpendicular to it. Polished sections of the hand blocks helped to define the geometry of deformation along

selected planes, as well as the protolith of the cataclasite. In any case, when possible, field work included measurement of foliation or tectonic banding in the fault rocks, and bedding in the footwall of the Rastraculos thrust (Fig. 2C).

4 RESULTS

In all sites the hangingwall consists of Middle Cambrian shales showing a pervasive Variscan foliation associated with asymmetric, north-verging folds and, striking NW-SE to E-W. In the footwall of the thrust, Mesozoic (Lower and Middle Triassic and Jurassic) beds gently dipping to the South, crop out. Below the Lower Triassic unconformity, vertically-dipping, strongly fractured Lower Cambrian conglomerates, with different facies and structure with respect to the Cambrian in the hanging wall, can be found. In spite of the differences in elevation or distance to the thrust surface, no systematic trend could be defined in the variation of lithology of the sampling sites. Although most of the deformation is concentrated in the fault zone, an asymmetric, north-verging fold having an E-W trend could be defined in the Jurassic limestones in the westernmost sampled outcrop.

Most fault rocks in the Rastraculos thrust can be classified as cohesive microbreccias, whose fragments range in size from 0.1 mm to several cm. Rock fragments can be often recognized according to their protolith (rarely Paleozoic, most commonly Triassic red beds and dolostones, and Jurassic limestones). Color differences (Table 1) imply different origins, since red sandstones and shales can be attributed to the Lower Triassic (Buntsandstein facies), yellow rocks to the Middle and Upper Triassic (Muschelkalk and Keuper facies) and grey microbreccia, usually limestone-based, derive from the Lower Jurassic beds.

4.1 Kinematic indicators

4.1.1. Outcrop and hand-sample scale

Although some sectors of the fault zone, associated with Triassic sandstones, or massive, Lower Jurassic limestones, do not show internal structures, in general, a foliation or tectonic banding is found throughout the Rastraculos fault zone, especially in fine-grained fault rocks. This foliation could be measured directly in the outcrop only in two cases (in RC1 and RC2), and observed in the hand samples and thin sections of the other outcrops (Fig. 3). Such foliation follows an E-W strike and shows an intermediate southwards dip (Fig. 2C), shallower than 45º in site RC1 and steeper in the rest of sites. At the outcrop scale, in RC2 site, calcareous breccia shows foliation, of pressure-solution origin (although a more chaotic facies dominates), with ESE-WNW strike and steep dips; scarce striae on fault planes indicate NNE transport direction (Fig. 2C). At the sample scale, in samples majoritarily derived from carbonatic rocks (either yellow Triassic dolostones or grey Jurassic limestones, Fig. 3C, E, G), foliation is defined by the alignment of anisometric clasts and it is more difficult to recognize, especially when the rock is strongly cemented (site RC5-A, Fig. 3C) and no pervasive discontinuities are found. However, in sample corresponding to site RC6-D (Fig. 3E) a well defined, SW steeply dipping (NW-SE striking) pressure-solution foliation surrounds a preserved clast of centimetric size, in which tension gashes with a ferruginous filling indicate stretching parallel to the dip direction of foliation. In fault rocks including fragments of Triassic red sandstones and shales, color bands usually define more clearly the foliation, and no pressure-solution features can be appreciated at the mesoscopic scale (Fig. 3D, F, H). These color bands represent finer grained (usually whitish or clearer) zones with microbreccia and fault gouge and coarser grained (yellow, red or grey) zones in which the protolith is still recognizable.

These coarse-grained zones can also show a finer matrix and oxydized fillings in tension gashes affecting the bigger clasts. In some of these samples, grains show a mixed origin between grey carbonates and red beds (site RC6-E, Fig. 3F). Although they cannot be inferred from outcrop observations, incipient shear planes with shallower dip than the general foliation can be interpreted from the polished section in site RC6-M (Fig. 3H). These shear planes are short and more rectilinear than foliation surfaces and generate roughly sigmoidal surfaces on the latter. Existence of shear planes can also be interpreted from sigmoidal shapes or the bimodal distribution of grain orientations in sample RC5-A (Fig. 3C). Finally, in one of the samples (site RC6-G, Fig. 3G) the foliation is affected by an asymmetric fold, consistent with a reverse shear, with top-to-the-NNE movement along the foliation surfaces.

In scarce sites, S-C structures are found, indicating a shallower dip for C planes, mostly observable in thin sections, but not so much in hand samples, where, as mentioned, only incipient shear surfaces can be defined (Figs. 3, 4, 5). At the outcrop scale, in RC2 site, calcareous breccia shows foliation of pressure-solution origin (although a more chaotic facies dominates). It strikes ESE-WNW strike and steep dips; scarce striae on fault planes indicate a NNE transport direction (Fig. 2C).

4.1.2. Microstructures

Observation of thin sections in different rock types indicates the existence of foliation and shear planes involving the microbreccia at the microscale. Although in a first approach, structures are difficult to recognize, at least when compared with other rock types, because of the coarse grain size, the detailed examination of thin sections provides clues to both the orientation of structures and the mechanisms of deformation involved in cataclasis and shear within the fault zone. Commonly recognized structures include (i) preferred

orientation of anisometric rock fragments, resulting from brecciation of both pelites (samples RC1-D15, RC6-A17, Figs. 4A, 5A) and limestones (samples RC3-B6, RC4-A14, Fig. 4C, D). (ii) Monomineralic quartz and calcite grains can also show preferred orientation (samples RC5-C, RC6-H1, Fig. 4E, F). (iii) In fault rocks derived from limestones (RC2-E3, Fig. 4B), foliation and shear planes are observed; foliation planes derive from pressure-solution surfaces with concentration of opaque minerals. These structures are consistent with reverse shear and top-to-the-North movement, with shallower dips for the shear planes and steeper for foliation. In other cases, shear planes can be inferred from the sigmoidal shapes of calcite grains (sample RC6-N, Fig. 5C). (iv) In most cataclasites, foliation and shear planes are not so common, and can be only defined from a rough foliation derived from orientation of milimetric rock fragments sharply cut by fragile shear planes having limited displacements (samples RC4-A14, RC6-H1, Fig. 4D, F, and sample RC5-A1, Fig. 5E, F). Shear planes are often inferred only from subtle deflections of grain orientation defining foliation planes (long axis of grains) when approaching the shear, sharper and planar surfaces. Other, more complex structures include (v) brittle grain elongation associated with tension gashes (sample RC6-G, Fig. 5B) and defining a stretching direction that usually follows the dip direction of foliation surfaces and the long axis of grains; and (vi) rotated grains consistent with reverse shear (samples RC6-N, RC6-O, Fig. 5C, D). Grain size of clasts in the analyzed thin sections is relatively homogeneous, ranging between a few milimeters to tens of microns. The matrix of the microbreccia consists mainly of calcite, small quartz grains and phyllosilicates (Figs. 3, 4, 5).

Opaque minerals appear either as (i) fine-grained (probably pigmentary) hematite contained in red pelites, whose fragments are oriented according to the general fabric of the rock (sample RC1-D15, Fig. 4A) or (ii) as concentrations along foliation surfaces often

deformed by shear planes (sample RC2-E3, Fig. 4B). In this case, concentrations of opaque minerals can be characterized as sheets with a bimodal distribution following shear planes and foliation planes. Moreover, pore filling by opaque minerals less than 0.3 mm in diameter are frequent in samples from RC5 and RC6 sites (Fig. 5). These particles can either show an individual shape anisotropy, with their long axes aligned according to foliation or shear planes or, alternatively, aggregates of several particles are the responsible for defining the foliation or the shear surfaces (sample RC6-N, Fig. 5C). Finally, secondary processes, such as filling of previous structures (foliation or shear planes) can be responsible for the distribution of opaque minerals and their mimicking of the compressional fabric (sample RC6-O, Fig. 5D).

4.1.3. Quantitative image analysis

In order to check the qualitative orientation of structures in thin section, quantitative image analysis was applied to the same thin sections, by means of Launeau and Robin (1996) and Launeau et al.'s (2010) method, as well as through the particle orientation analysis tool provided by the ImageJ program. From this analysis it can be seen that (i) orientation of the resulting equivalent ellipse follows an orientation similar to the one determined from direct observation of the foliation and the shear planes, being an intermediate between both sets of surfaces when shear planes are well developed, and that (ii) the anisotropy degree is very low in most of the samples (low eccentricity of the equivalent ellipses), what agrees with the weak orientation and scarcity of structural markers that can be observed in most of the cataclasites.

4.1.4. Summary of tectonic fabrics and kinematic indicators

The main observed fabrics can be summarized in: i) a foliation with an E-W to NW-SE overall strike and intermediate southwards dip, parallel or slightly oblique to the fault trace,

measured directly in the outcrop (RC1 and RC2 sites), in hand samples (RC5 and RC6 sites) and thin section (all sites); ii) in scarce sites, shear planes are found, showing a similar strike and a shallower dip than foliation, mostly observable in thin sections (Figs. 4, 5), but not so much in hand samples, where, as mentioned, only incipient shear surfaces can be defined (RC5-A and RC6-M sites, Fig. 3C, H); iii) fractured grains and tension gashes perpendicular to foliation in hand sample and thin section (Fig. 3C, E, F, H, Fig. 5B); iv) asymmetric folds in hand sample (RC6-G site, Fig. 3G); v) scarce striae on fault planes in the outcrop (RC2 site, Fig. 2C). The orientation and characteristics that define the foliation and the shear planes and their geometrical relationship allows us to interpret it as reverse S-C' structures with top-to-the-North movement, consistently with the mapped trace of the Rastraculos thrust and its reconstruction in cross-section.

4.2 Magnetic mineralogy

Magnetic susceptibility of studied specimens of the Rastraculos fault zone varies between -2.25x10^{-6} (slightly diamagnetic values) and 307x10^{-6} SI (Fig. 6A); 85% of the specimens show values of Km above 50 x10^{-6} SI, and only 2 samples out of 46 (4%) show an average Km value below 50 x10^{-6} SI (Table 1).

Thermomagnetic analyses (k-T curves) can be grouped into two types: (1) Strongly decreasing hyperbolic shape at the beginning of the heating curve (more than 80% paramagnetic contribution, according to estimation by the method of Hrouda *et al.*, 1997) for the analyzed samples. This group includes samples RC1-G22, RC3-C26, RC5-C, RC6-H28, RC6-O11 (Fig. 6B, D). 2) Moderately decreasing hyperbolic shape at the beginning of the heating curve (less than 70% of paramagnetic contribution, Hrouda *et al.*, 1997) for RC5-A and RC6-A (Fig. 6C). Furthermore, an abrupt increase in susceptibility at 500ºC evidences the neoformation of magnetite during heating in four of the analyzed samples

(RC2-D, RC5-A, RC5-C and RC6-A, Fig. 6C). Moreover, curves are not reversible, and cooling paths show susceptibilities one order of magnitude higher than heating paths, confirming the formation of ferromagnetic phases during heating. Finally, the fall of susceptibility at higher temperatures indicates the presence of hematite in all of the studied samples (Fig. 6B, C, D), although its amount is very small in type 1 curves (Fig. 6B).

In order to verify the presence of primary hematite, four selected specimens (including those representing the two types of k-T curves: RC1-A6, RC1-A10, RC6-E22 and RC6-A10) were subjected to remanence rock magnetic experiments. These experiments indicate the presence of high coercivity ferromagnetic minerals s.l. (Fig. 6E), characterized both by high coercivities (150-200 mT; Fig. 6E) and by high remanent coercivities (~ 400 mT; Fig. 6F). Magnetization thermomagnetic curve (Fig. 6G) is mostly reversible with a single phase showing Néel temperature around 680ºC. All these features agree with the presence of hematite as the main ferromagnetic mineral in the measured samples for both types of k-T curves obtained (Dunlop & Özdemir 1997).

4.3 Magnetic fabrics

Global results of orientation distribution of AMS axes reflect a strong scattering derived from the high number of data (more than one thousand measured samples, Fig. 7A). Nevertheless, two main patterns of k_{max} (shallow plunging ESE-WNW trend and intermediate to steep plunging, SW trend) and k_{min} (distribution within a NNE vertical girdle), can be distinguished (Fig. 7B). The corrected degree of anisotropy (Pj) is mostly concentrated below 1.08 and it does not seem to depend on the magnetic susceptibility (Km/Pj diagram in Fig. 7C). Although the three types of ellipsoid shapes (oblate, prolate and triaxial) co-exist in the studied samples, there is a dominance of oblate ellipsoids. As occurring in other fault zones, there is a certain relationship between the shape of the

ellipsoid and the degree of anisotropy, the latter increasing in strongly oblate ellipsoids with respect to the triaxial and, especially, prolate shapes (Pj/T diagram in Fig. 7C).

The particular orientation of magnetic axes in each of the six analyzed sites shows differences in both geometry and distribution of the three main axes of the magnetic anisotropy ellipsoid and their relative clustering or scattering (Fig. 8), that is usually related to the degree of anisotropy and their shape parameter (Fig. 9). The six analyzed sites can be grouped in three main orientation patterns (types, Fig. 8) explained in the following lines. Sites RC1 and RC3 show a Type 1 fabric, characterized by a steeply-plunging cluster of k_{min} axes (corresponding thus with shallow-dipping magnetic foliation) and a mostly horizontal k_{max} (magnetic lineation), with a strong scattering in trend (from E-W to NW-SE). An incipient scattering of k_{max} within the girdle corresponding to the magnetic foliation can also be distinguished (Fig. 8A). Sites RC2 and RC4 (projected together in the stereoplot of Fig. 8B) show the Type 2 fabric, defined by a fairly clustered horizontal k_{max} in WNW-ESE direction (in spite of the dominance of oblate magnetic ellipsoids at the sample scale) and a more scattered k_{min}, that shows an average in NE-SW horizontal position. Some of the samples do not fit into this directional pattern (for example, subvertical k_{min} or subhorizontal k_{min} in E-W direction are also found) but they do not show differential scalar features and therefore we have considered them as anomalous samples that do not interfere with the robust average, defined by the largest number of samples.

Samples from RC5 site appear in different stereoplots according to their axes orientation pattern (types 2 and 3 fabrics, Fig. 8B, C). RC5-C samples show k_{min} distributed within a NNE-SSW vertical girdle, although the maximum is still horizontal (vertical magnetic foliation), as in RC2 and RC4 (Type 2 fabric). In this case, k_{max} is very well defined, showing a N100E trend with a subhorizontal plunge (Fig. 8B). Conversely, RC5-A and

RC5-B, that contain more dark/opaque grains (see Fig. 3C), show a completely different orientation pattern (Type 3 fabric), with k_{min} distributed within a NW-SE, north-dipping girdle, and k_{max} clustered around 213/47 and 227/41, respectively (Fig. 8C and Table 2). As in sites RC2 and RC4, this variation is not related to a particular anisotropy degree or shape of the magnetic anisotropy ellipsoid, since samples with similar axes orientation cover all the range of values of these parameters. A similar situation is found in site R6, that can be divided into two groups (corresponding to types 2 and 3 fabrics): (i) samples RC6-E, RC6-H and RC6-L show horizontal k_{max} and horizontal k_{min} (vertical magnetic foliation) with well-defined maxima in WNW-ESE and NNE-SSW directions, respectively (Type 2 fabric, Fig. 8B); (ii) the rest of samples (except for R6-O, that shows a completely different pattern, and a more greenish lithology, see Fig. 8C) show k_{min} distributed within a NE-dipping girdle, and SW-trending, steeply-plunging k_{max} axes (Type 3 fabric, Fig. 8C). These latter show low degrees of anisotropy at the sample scale, and a variety of ellipsoid shapes (both prolate and oblate, Fig. 9C). However, the shape parameter is not a defining element, since oblate ellipsoids are also found in samples of both types (RC6-H and RC6-M, for example).

In summary, orientation distribution of AMS axes (Fig. 8) shows three main patterns: 1) Type 1 shows a strong clustering of k_{min} axes in an NNE direction and high to intermediate plunges (shallow-dipping magnetic foliation), accompanied by a strong clustering of k_{max} axes in an ESE-WNW horizontal direction (RC1 and RC3, Fig. 8A), 2) Type 2 is characterized by a concentration of k_{max} in the same ESE-WNW direction and dispersion of k_{min} along a vertical, great circle perpendicular to it, with maximum of horizontal plunges (subvertical magnetic foliation, RC2, RC4, RC5-C and RC6-E, H, L, Fig. 8B), and 3) finally, Type 3 shows a clustering of k_{max} axes around a SW trend with strong inclination

and distribution of k_{min} axes within a great circle whose pole is k_{max} (RC6-A, C, D, F, G, J, K, M and N, Fig. 8C). Additionally, a fourth pattern can be described, very similar to Type 3 regarding axis distribution, but with lower inclination of k_{max} (RC5-A and B) or even horizontal k_{max} (RC6-O).

Some of the described types can coexist within the same site, as it occurs in the RC1 site, where both horizontal (parallel to the strike of the magnetic foliation) and shallowly plunging lineations, following the dip direction of the magnetic foliation coexist. The dip of the magnetic foliation can also change between sites, from subhorizontal (site RC3) to subvertical (sites RC2, RC4 and RC6-E, H and L). The different types of fabrics (namely types 2 and 3) can also coexist in near sites (RC5-A and 5B for Type 3 fabric *vs.* RC5-C for Type 2 fabric). Interestingly, the trends of lineation in the majoritary fabrics are perpendicular to the transport direction, whereas foliations show a majoritary WNW-ESE strike, except for some samples in sites RC5-A and B and RC6-O that show a NNE-SSW strike.

Regarding scalar parameters (Fig. 9), in RC1 site, a positive correlation between the magnetic susceptibility (showing values between -2.25×10^{-6} and 307×10^{-6} SI) and the corrected anisotropy degree is found, with most samples concentrating in a narrow band of strongly oblate ellipsoids and relatively high anisotropy degree (Fig. 9A). Conversely, in sites RC2, RC3 and RC4, where magnetic susceptibility is lower (between 9.27×10^{-6} and 168×10^{-6} SI) a negative correlation between the two parameters is found (Fig. 9A, B), and strongly oblate ellipsoids having very low degree of anisotropy are dominant. In RC5 site, averaged susceptibility is lower (between 19.2×10^{-6} and 107×10^{-6} SI), and the degree of anisotropy rather low, with a more even distribution between prolate and oblate ellipsoids

(Fig. 9B, C). Finally, in RC6 sites, low susceptibility values (between 20.5×10^{-6} and 234×10^{-6} SI) coexist with a strong variability in the degree of anisotropy and shape of the magnetic susceptibility ellipsoids, although oblate shapes are still majority (Fig. 9B, C).

AMS measurements at low temperature indicate that the increase in bulk susceptibility with respect to room temperature corresponds to a factor of 3.1 for site RC1, 2.19 for site RC6-E-H-L and 2.36 for site RC6-A-C-J-M-N (Fig. 10A). Such ratios (lower than 3.8 and above 1) indicate a partial contribution of ferromagnetic phases to the susceptibility, and the higher ratio for RC1 indicates that the contribution of paramagnetic phase is higher in this site, corroborating k-T results (see Fig. 6B). The magnetic axes of samples from sites RC1 and RC6-E-H-L remain unchanged in orientation at low temperature with respect to the room temperature measurements, while in site RC6-A-C-J-M-N the overlapping is not so good (Fig. 10B). The overlapping of LT-AMS and RT-AMS in sites RC1 and RC6-E-H-L (Fig. 10B) indicates that paramagnetic contribution dominates RT-AMS in these sites, which present Type 1 and Type 2 magnetic fabrics (see Fig. 8). Alternatively, it can also mean that the paramagnetic and the ferromagnetic contributions have the same fabric. On the other hand, samples RC6-A-C-J-M-N, where overlapping is not so good, present somewhat higher ferromagnetic contribution (see Fig. 6C) and a Type 3 magnetic fabric (see Fig. 8).

5 INTERPRETATION AND DISCUSSION

5.1. Interpretation of magnetic fabrics: geometrical constraints

In spite of the scarcity of kinematic indicators at the outcrop scale (Figs. 2C and 3A, B), the characterization of deformational structures under the microscope and in hand-sample polished sections (20 thin sections observed under the microscope and 18 polished sections

plus direct observations on the faces of cubes cut for AMS measurement, see Figs. 3, 4, 5) provides major constraints to establish relationships between the magnetic fabrics, the petrofabric and the transport direction for shear structures, site by site and in the Rastraculos fault zone as a whole.

In RC1 and RC3 (fabrics of Type 1, having a well-defined foliation), magnetic foliation, with shallow dips (average 30º or less for both sites, Fig. 8A) coincides with the foliation observed in polished and thin section. For fabrics of Type 2 (sites RC2, RC4, RC5-C, RC6-E, H, L), with steep dips of the foliation (subvertical average, Fig. 8B) there is also a coincidence between the observed (wherever was possible to assess the orientation of foliation from thin and polished sections) and the magnetic foliation. It is interesting to note that in sites showing a weakly-defined foliation whose poles are distributed along a girdle (for example, RC5-C, Fig. 8B) observations in thin section also show an unclear distribution in the orientation of rock fragments (Fig. 4E). In general, in sites showing shallow-dipping foliation, shear planes cannot be identified (sites RC1 and RC3), and, conversely, when foliation shows steep dips (sites RC2, RC4, RC5-C and RC6-E, H, L, see Figs. 3, 4, 5), shear planes are more easily identified in thin sections, what points to a simple, co-genetic relationship (according to NNE-directed reverse faulting) between foliation and shear planes.

In samples where they co-exist, conforming (sometimes poorly-defined) the classical pattern of S-C' structures, foliation and shear planes are consistent with a NNE transport direction (i.e. both of them show an E-W to WNW-ESE strike). Exceptions are sites where shear planes cannot be defined (for example, the above-mentioned site RC1, where only a shallow dipping foliation, associated with strong deformation, can be seen). In this case, C' planes are not individualized both in horizontal and vertical sections, but instead, we can

establish a coincidence between shear and foliation planes, inferred from the strong deformation at grain scale. This kind of deformational pattern and its relationships with magnetic fabrics have also been found in other fault rocks (gouge and microbreccia) formed at shallow depths (Casas-Sainz et al., 2018). When S-C' structures can be defined, the fact that they can be recognized only in vertical sections (and not in sections containing the horizontal line) is an indication of C' planes having a strike parallel to the S planes or main orientation of clasts.

Although the origin of the magnetic foliation is interpreted in different ways for Type 1 and Type 2 fabrics, the coincidence in the orientation of the magnetic lineations allows to claim for a common origin for these lineations. The horizontal magnetic lineation obtained in the Rastraculos fault zone for both types 1 and 2 (Fig. 11) must therefore show a strong parallelism with the intersection lineation between S and C' planes, observed in site RC2 (Fig. 4B), and inferred in sites RC4 and RC6 (Fig. 4D, F). The thrust transport direction is in this case perpendicular to the magnetic lineation, as has also been interpreted in other intraplate fault zones dominated by paramagnetic fabrics (Casas-Sainz et al. 2018). The fact that magnetic lineation is ESE-WNW, slightly oblique to the strike of the thrust in this area (practically W-E), implies a slight left-lateral strike-slip component in the movement of the thrust. However, and probably because of the slight obliquity, this sinistral transpressional component is not reflected in thin sections containing the horizontal in the studied samples. In other cataclastic fault zones (Casas-Sainz *et al.* 2017, 2018), steep magnetic foliations have been interpreted as corresponding to foliation planes whereas shallower dipping magnetic foliations are considered as shear surfaces, difficult to observe at the outcrop scale but present in thin sections. However, in the Rastraculos thrust, for Type 1 magnetic fabrics, the interpreted parallelism between foliation and shear surfaces derived from

stronger deformation (probably because of concentration of a similar shortening within a narrower shear band) also facilitates a more strict correspondence between magnetic foliation and the foliation defined from polished sections and thin-section observations.

As already mentioned, for Type 3 fabrics, represented mainly in sites RC5 and RC6 (thin sections shown in Fig. 5), the relationship of magnetic fabrics with deformation axes is more complicated. In spite of showing majoritarily oblate fabrics at the sample scale, k_{min} axes define altogether a great circle whose pole is the magnetic lineation (Fig. 8C), which is parallel to the transport direction projected onto the visible SW steeply dipping foliation planes (Fig. 11). This transport direction is consistent, on the other hand, with the transport direction obtained in fabrics of types 1 and 2 in RC5 and RC6, and the rest of the sites. This relationship is clear for RC6 (samples A, C, D, F, G, J, K, M, N) site, where the average magnetic lineation shows steep plunges, which are much lower in RC5 (A and B) and finally horizontal in RC6-O.

5.2 Interpretation of magnetic fabrics: lithological and mineralogical constraints

These differences in axes orientation are difficult to interpret in terms of varying deformation (or shear) intensity, because Type 3 fabrics are not related to particular deformational features with respect to the other types (as inferred from polished and thin section observation, Figs. 3, 4, 5), and the same occurs between types 1 and 2.

Let us first consider differences between types 1 and 2, namely the orientation of the magnetic foliation. Although there are not differences in the anisotropy degree, Pj, between types 1 and 2, significant differences in the observations of thin sections point to different deformation mechanisms and geometrical relationships between foliation and shear planes. Whereas in Type 2 foliation planes are subvertical and can be separated from discrete, shallowly-dipping shear planes, deformational features found in rocks corresponding to

Type 1 fabric (grain elongation, lozenge-shaped grains, etc…) point to a stronger deformational pattern and parallelism between the two sets of surfaces, thus acquiring a dip angle that approaches that of the shear planes, clearly reflected in the magnetic fabric.

Alternatively (although both factors are compatible and do probably co-exist), a lithological constraint can be put up to explain the difference in foliation orientation between the two magnetic fabric types. Magnetic fabrics in limestones (more represented in Type 2 fabrics with respect to Type 1, see Table 1 in which sites RC1 show higher proportion of red shales) are often prolate (both at the sample scale and in site averages) whereas the presence of phyllosilicates usually gives a more oblate character to the magnetic ellipsoid. Another alternative explanation, also related to lithology, would be the poor orientation of clasts in Type 2 fabrics, and hence the weak definition of foliation, as evidenced, for example, in image analysis of the thin sections. Under cataclastic deformation conditions, grains of different size are rotated and their long axes often mimic the shear, rather than the foliation planes (feature visible in both Figs. 4 and 5). However, this is in contradiction with the more intense shear appearing in some samples, associated with grain rotation (Fig. 4B, F) that are not apparently related to changes in the magnetic fabric with respect to other samples. In this case, the explanation is two-fold: mineralogy of the involved grains (diamagnetic in both cases, calcite and quartz, respectively) and the brittle character of shear planes. Regarding magnetic mineralogy, for Type 1 and Type 2 magnetic fabrics (corresponding to thin sections shown in Fig. 4) no distinction in orientation can be established between the different components of the rock: hematite, for example is contained either in red pelites oriented according to the general fabric of the rock (Fig. 4A) or as concentrations within foliation surfaces deformed by shear planes (Fig. 4B). In these cataclasites, no other opaque minerals, apart from those described and some

coatings around grains can be visually distinguished.

Magnetic mineralogy can also give a clue about the differences between types 1 and 2 (that show similarities regarding this issue) vs. Type 3 fabrics, since the former show a higher relative contribution of paramagnetic vs. ferromagnetic minerals to the total susceptibility (as shown, for example, in other fault zones having a horizontal magnetic lineation by Casas-Sainz et al. 2018). This difference can be interpreted as follows: ferromagnetic fabrics identifying magnetic lineation with the transport direction (projected onto the magnetic foliation plane), vs. paramagnetic-dominated fabrics providing magnetic lineation perpendicular to the transport direction in the fault zone. The particular ferromagnetic minerals and their habits, though, should be taken into account, because of the different behavior of planar and granular hematite in AMS results. Planar hematite included in brecciated shales and oriented within the fault zone would probably give planar magnetic fabrics whose magnetic foliation is parallel to the petrofabric foliation and a magnetic lineation parallel to the intersection lineation. Conversely, granular hematite (and possibly other ferromagnetic *s.l.* minerals), oriented within similarly deformed rocks can be responsible for linear fabrics corresponding to Type 3. The heterogeneous spatial distribution of grains can also have an influence because small grains and pore fillings of opaque minerals less than 0.3 mm in diameter are specially frequent in Type 3 fabrics (Fig. 5) with respect to types 1 and 2 (Fig. 4). These differences, and the relative contribution of para- and ferro-magnetic fractions to the total susceptibility, can explain the different types of fabrics found (Fig. 11).

In the studied samples, no strong differences seem to exist according to the matrix and the clast composition: i.e. types 1, 2 and 3 appear indistinctly in rocks with different colors (and hence protoliths) or containing pelites or limestone fragments. This indicates that,

strictly speaking, the lithological factor or the previous, sedimentary (presumably weak) fabric of rocks does not significantly influence the orientation of the magnetic ellipsoid.

All in all, the studied case reveals that the relationship between AMS axes and deformation in fault zones must be carefully checked by means of thin section observations and application of other complementary techniques (in this case, LT-AMS). Relationship between the kinematics of the fault and AMS axes is indicated by the identification of magnetic lineation either with the intersection lineation between shear and flattening (magnetic foliation) planes or with the transport direction projected onto S (magnetic foliation) planes. A high number of samples (more than one thousand in this case) is a guarantee of the accuracy of the results and the acquisition of statistically robust means, that allow for a good approximation to deformation axes even in absence of conventional kinematic markers.

6 CONCLUSIONS

The application of Anisotropy of Magnetic Susceptibility to fault rocks of the Rastraculos thrust (Cameros-Demanda massif, Iberian Chain) provides consistent results in the different studied outcrops (six sites). The magnetic foliation is related to the tectonic foliation found in thin and polished sections in Type 2 fabrics, whereas in Type 1 fabrics shear and foliation planes show similar attitudes (consistent with the magnetic lineation), related to higher deformation degree. The results obtained allow to infer the transport direction of the thrust, either perpendicular to magnetic lineation (that coincides with the intersection lineation in Type 1 and Type 2 magnetic fabrics) or from the projection of magnetic lineation (in Type 3 magnetic fabrics) onto the shear planes. Note that, strictly speaking, to obtain the transport direction, we must always project the magnetic lineation (in cases where it is “transport-parallel”) or its perpendicular (in cases where it is “transport-

perpendicular" onto the shear planes (or the assumed orientation of the thrust plane inferred from macrostructural observations), in spite that, originally, the magnetic lineation is contained within the foliation plane.

Kinematic implications are the existence of a main dip-slip component for the main segment of the thrust, that could show a slight strike-slip component (not evident from outcrop, sample or thin section observations) derived from the obliquity of the transport direction (N to NNE) and the mapped thrust trace. This transport direction is slightly oblique (probably conditioned by structural trends inherited from Variscan and Late-Variscan times) with respect to the main direction obtained for the Cameros-Demanda thrust (NNW according to Casas *et al.* 2017), but almost perpendicular to the main compression direction in the northwestern Iberian Chain (Casas-Sainz et al. 1992). This implies the necessity for considering the influence of the orientation of faults inherited from the Late-Variscan stage, intra-hangingwall structures, and their displacement vectors (not necessarily coaxial) to obtain a reliable picture and restoration of compressional movements in intra-plate thrusts. Finally, we interpret that magnetic mineralogy, and possibly the habit of hematite, that is partly related to rock fault provenance, is the main factor influencing the type of magnetic fabric obtained, rather than the intensity of deformation at the outcrop scale.

ACKNOWLEDGEMENTS

The authors are grateful to Pedro Silva and an anonymous referee for their thorough revision of the manuscript, and to the Servicio General de Apoyo a la Investigación-SAI (Servicio de Preparación de Rocas y Materiales Duros and Servicio de Líquidos Criogénicos) and Sylvia Gracia (Earth Sciences Department) of the University of Zaragoza for their help in processing samples and measuring AMS. Financial support was granted by

projects CGL2013-42670-P of the MINECO (Ministerio de Economía y Competitividad of Spain) and Geotransfer-E32_17R of the Gobierno de Aragón y Programa Operativo FEDER Aragón 2014-2020.

REFERENCES

Allmendinger, R.W., Cardozo, N.C. & Fisher, D., 2013. *Structural geology algorithms: vectors & tensors*. Cambridge University Press, Cambridge.

Braun, D., Weinberger, R., Eyal, Y., Feinstein, S., Harlavan, Y. & Levi, T., 2015. Distinctive diamagnetic fabrics in dolostones evolved at fault cores, the Dead Sea Transform. *Journal of Structural Geology,* **77,** 11-26.

Cardozo N. & Allmendinger R.W., 2013. Spherical projections with OSXStereonet. *Comput. Geosci.,* **51**, 193-205.

Cámara, P. & Durantez, O., 1978. *Mapa Geológico de España a escala 1:50.000. Hoja 279-Villoslada de Cameros*. Instituto Geológico y Minero de España, Madrid, 38 p., 1 map.

Casas, A. M., Simon, J. L., & Seron, F. J. (1992). Stress deflection in a tectonic compressional field: a model for the Northwestern Iberian Chain, Spain. *Journal of Geophysical Research: Solid Earth*, **97(B5)**, 7183-7192.

Casas-Sainz, A. M. & Gil-Imaz, A., 1998. Extensional subsidence, contractional folding and thrust inversion of the eastern Cameros basin, northern Spain. *Geologische Rundschau*, **86** (4), 802-818.

Casas-Sainz, A.M., Román-Berdiel, T., Oliva-Urcia, B., García-Lasanta, C., Villalaín, J.J., Aldega, L., Corrado, S., Caricchi, C., Invernizzi, C. & Osácar, M.C., 2017. Multidisciplinary approach to constrain kinematics of fault zones at shallow depths: a case study from the Cameros–Demanda thrust (North Spain). *International Journal of Earth Sciences,* **106,** 1023-1055.

Casas-Sainz, A. M., Gil-Imaz, A., Simón, J. L., Izquierdo-Llavall, E., Aldega, L., Román-Berdiel, T., Osácar, M.C., Pueyo-Anchuela, O., Ansón, M., García-Lasanta, C., Corrado, S., Invernizzi,

C. & Caricchi, C., 2018. Strain indicators and magnetic fabric in intraplate fault zones: Case study of Daroca thrust, Iberian Chain, Spain. *Tectonophysics*, **730**, 29-47.

Chadima, M. & Hrouda, F., 2009. Cureval 8.0: Thermomagnetic Curve Browser for Windows. *Agico, Inc.*

Chadima, M. & Jelinek, V., 2009. Anisoft 4.2: Anisotropy Data Browser for Windows. *Agico, Inc.*

Colchen, M., 1974. *Géologie de la Sierra de la Demanda Burgos-Logrono (Espagne)* (Vols. 1, 2). Instituto Geológico y Minero de España, Madrid, 436 p.

Dunlop, D.J. & Özdemir, Ö., 1997. Rockmagnetism: fundamentals and frontiers, in *Cambridge Studies in Magnetism*, Cambridge University Press, Cambridge, pp. 573.

Gil-Serrano, G., Jiménez Benayas, S. & Zubieta Freire, J.M., 1977. *Mapa Geológico de España a escala 1:50.000. Hoja 278-Canales de la Sierra*. Instituto Geológico y Minero de España, Madrid, 43 p., 1 map.

García-Lasanta, C., Oliva-Urcia, B., Román-Berdiel, T., Casas, A.M. & Pérez-Lorente, F., 2013. Development of magnetic fabric in sedimentary rocks: insights from early compactional structures (ECS). *Geophysical Journal International,* **194** (1), 182–199.

Guimerà, J. & Alvaro, M., 1990. Structure et évolution de la compression alpine dans la Chaîne Ibérique et la Chaîne côtière catalane (Espagne). *Bull. Soc. Géol. Fr.,* **8,** 339-348.

Hrouda, F., Jélinek, V. & Zapletal, K., 1997. Refined technique for susceptibility resolution into ferromagnetic and paramagnetic components based on susceptibility temperature-variation measurement. *Geophys. J. Int.,* **129,** 715-719.

Issachar, R., Levi, T., Lyakhovsky, V., Marco, S. & Weinberger, R., 2016. Improving the method of low-temperature anisotropy of magnetic susceptibility (LT-AMS) measurements in air. *Geochemistry, Geophysics, Geosystems - G3,* **17, 7,** 2940-2950.

Jelinek, V., 1978. Statistical processing of anisotropy of magnetic susceptibility measured on groups of specimens. *Studia Geophysica et Geodetica,* **22,** 50-62.

Jelinek, V., 1981. Characterization of the magnetic fabric of rocks. *Tectonophysics,* **79,** 63-70.

Keskineva, A., Georgiev, N., Naydenov, K., Jordanova, N., Jordanova, D. & Dimowa, L., 2016. Magneto-structural and mineralogical study of tectonic gouge. Bulgarian Geological Society, *National Conference with international participation "Geosciences 2016"*, 89-90.

Launeau, P. & Robin, P.Y., 1996. Fabric analysis using the intercept method. *Tectonophysics*, **267**, 91-119.

Launeau, P., Archanjo, C.J., Picard, D., Arbaret, L., & Robin, P.Y., 2010. Two-and three-dimensional shape fabric analysis by the intercept method in grey levels. *Tectonophysics*, **492**, 230-239.

Levi, T., Weinberger, R. & Marco, S., 2014. Magnetic fabrics induced by dynamic faulting reveal damage zone sizes in soft rocks, Dead Sea basin. *Geophys. J. Int.,* **199,** 1214-1229.

Liesa Carrera, C.L. & Casas Sainz, A.M., 1994. Reactivación alpina de pliegues y fallas del zócalo hercínico de la Cordillera Ibérica: ejemplos de la Sierra de la Demanda y la Serranía de Cuenca. *Cuadernos do Laboratorio Xeolóxico de Laxe*, **19**, 119-136.

Lüneburg, C.M., Lampert, S.A., Hermann, I., Lebit, D., Hirt, A.M., Casey, M. & Lowrie, W., 1999. Magnetic anisotropy, rock fabrics and finite strain in deformed sediments of SW Sardinia (Italy). *Tectonophysics,* **307,** 51-74.

Martín-Hernández, F. & Ferré, E.C., 2007. Separation of paramagnetic and ferromagnetic anisotropies: a review. *Journal of Geophysical Research-Solid Earth,* **112 (B3),** B03105.

Mertainen, S. & Karell, F. 2012. Palaeomagnetic and AMS studies on Satulinmäkiand Koijärvi fault and shear zones. *Geological Survey of Finland, Special Paper,* **52,** 195–226.

Moreno, E., Homberg, C., Schnyder, J., Person, A., du Peloux, A.& Dock, P., 2014. Fault imprint in clay units: magnetic fabric, structural and mineralogical signature. *EGU General Assembly 2014. Geophysical Research Abstracts,* **16,** EGU2014-15479.

Oliva-Urcia, B., Román-Berdiel, T., Casas, A.M., Pueyo, E.L. & Osácar, C., 2010. Tertiary compressional overprint on Aptian-Albian extensional magnetic fabrics, North Pyrenean Zone. *Journal of Structural Geology,* **32,** 362-376.

Pomella, H. (2014). Magnetic fabic of brittle fault rocks. *EGU General Assembly 2014. Geophysical Research Abstracts* **16,** EGU2014-12505.

Parés, J.M. & van der Pluijm, B.A., 2002a. Evaluating magnetic lineations (AMS) in deformed rocks. *Tectonophysics,* **350,** 283-298.

Parés, J.M. & Van der Pluijm, B.A., 2002b. Phyllosilicate fabric characterization by Low-Temperature Anisotropy of Magnetic Susceptibility (LT-AMS). *Geophys. Res. Lett.,* **29 (24)**. doi:10.1029/2002GL015459

Petrovsky, E. & Kapicka, A., 2006. On determination of the Curie point from thermomagnetic curves. *Journal of Geophysical Research,* **11,** B12S27. doi:10.1029/2006JB004507

Ritcher, C. & Van der Pluijm, B.A., 1994. Separation of paramagnetic and ferrimagnetic susceptibilities using low temperature magnetic susceptibilities and comparison with high field methods. *Physics of the Earth and Planetary Interiors,* **82,** 113-123.

Solum, J.G. & Van der Pluijm, B.A., 2009. Quantification of fabrics in clay gouge from the Carboneras fault, Spain and implications for fault behavior. *Tectonophysics,* **475 (3),** 554-562.

Soto, R., Casas-Sainz, A. M., Villalaín, J. J., Gil-Imaz, A., Fernández-González, G., Del Río, P., Calvo, M. & Mochales, T. (2008). Characterizing the Mesozoic extension direction in the northern Iberian plate margin by anisotropy of magnetic susceptibility (AMS). *Journal of the Geological Society*, **165,** 1007-1018.

Yenes, M., Alvarez, F. & Nieto, F., 1990. Análisis estructural y metamórfico de la deformación hercínica del borde meridional de la Sierra de la Demanda. *Estudios Geológicos*, **46** (3-4), 223-236.

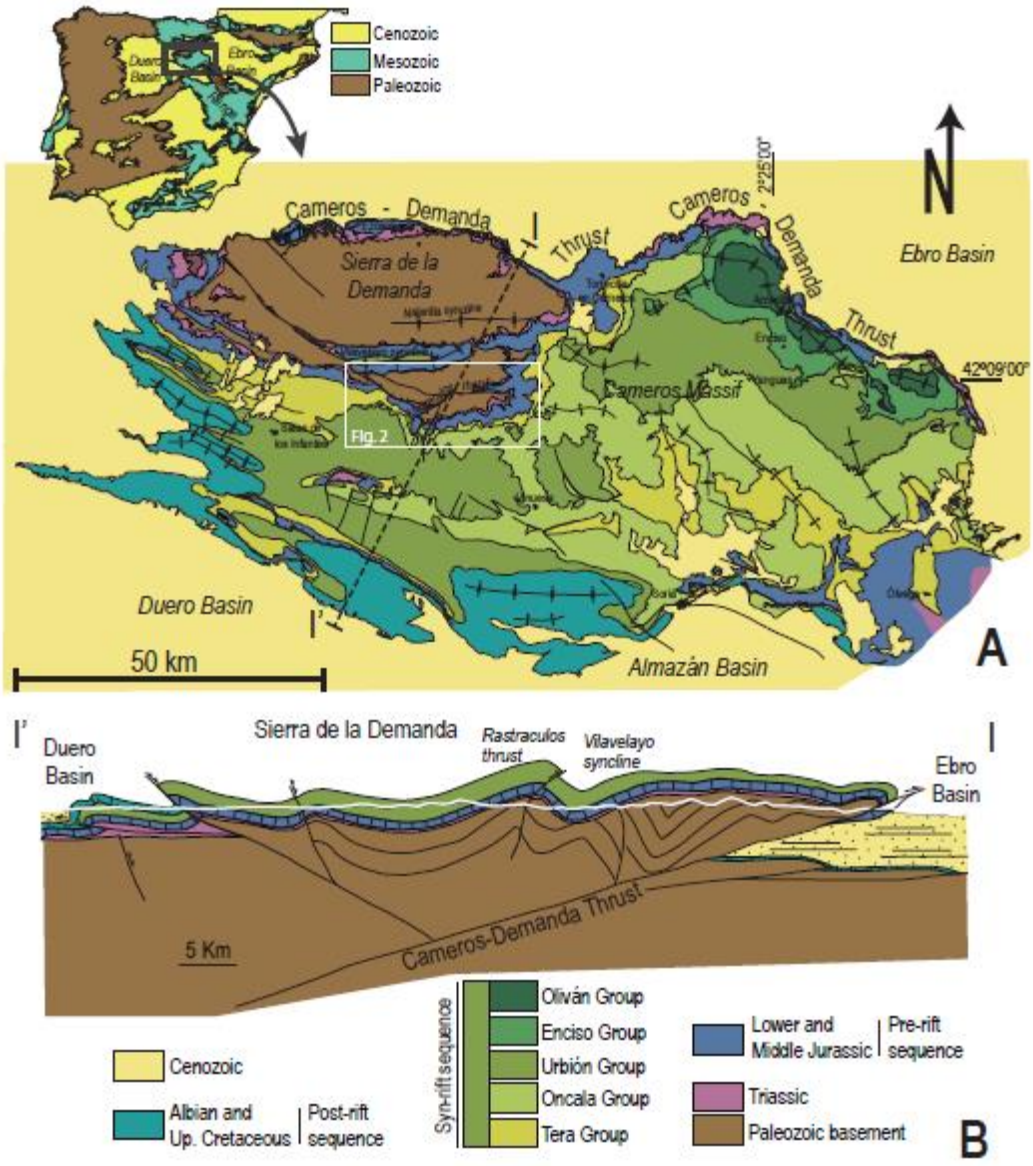

Figure 1. Location of the studied area (A) within the Cameros-Demanda Massif (modified from García-Lasanta *et al.* 2013), and cross section (B) showing the overall structure of the Sierra de la Demanda (modified from Casas-Sainz *et al.* 2017).

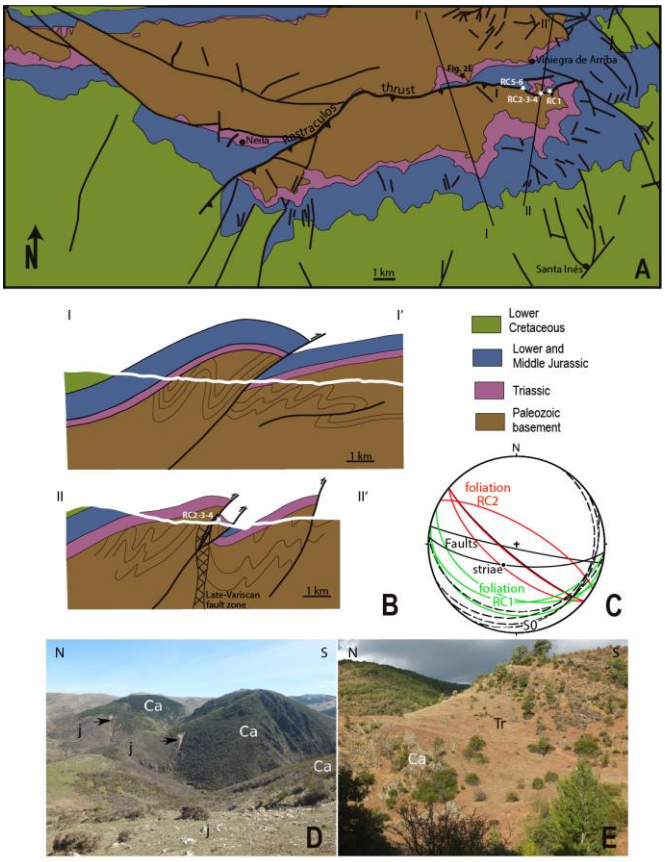

Figure 2. A. Geological sketch of the Rastraculos thrust area (modified from Cámara & Durantez 1978 and Gil Serrano *et al.* 1977). The location of sampling sites for AMS and thin section analysis is shown. B. Cross-sections of the Rastraculos thrust. C. Stereoplot showing orientation of kinematic indicators measured in outcrop (lower hemisphere, Schmidt projection, Stereonet software, Allmendinger et al. 2013; Cardozo & Allmendinger 2013), S0: bedding. D. Panoramic view of the Rastraculos thrust near its eastern termination, j: Jurassic limestones, Ca: Cambrian sandstones, shales and limestones. Arrows indicate the trace of the thrust, underlined by outcrops of fault breccia (the one in the foreground corresponds to RC2, RC3 and RC4 sites). E. Field aspect of the footwall of the Rastraculos thrust (Triassic/Paleozoic unconformity in the Urbión valley).

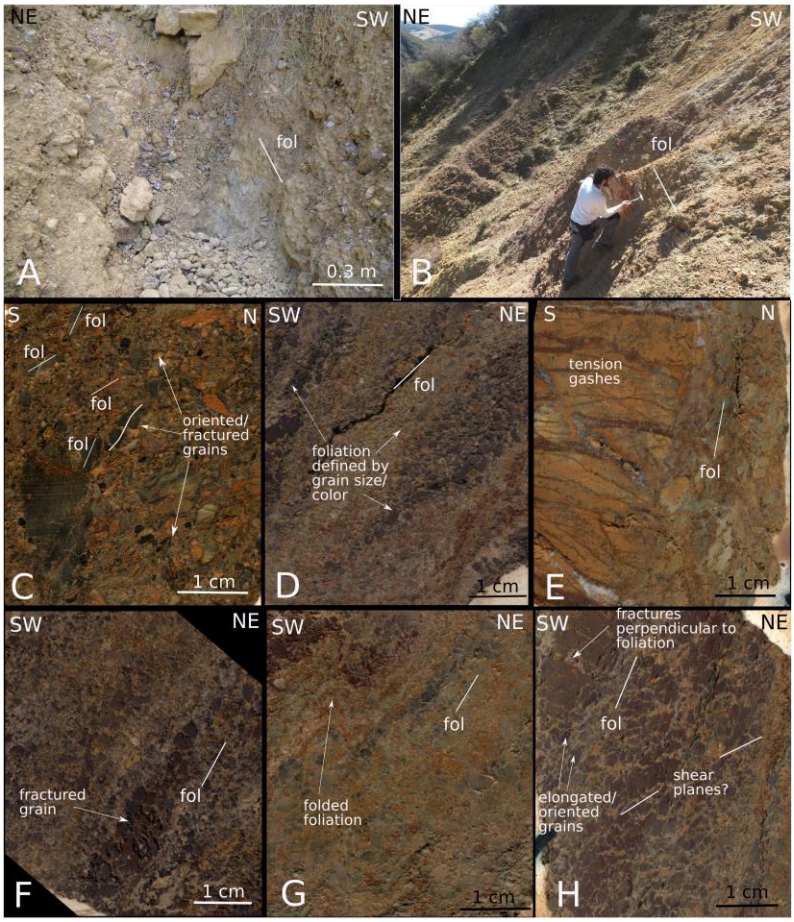

Figure 3. Outcrop aspects of the fault rocks of the Rastraculos thrust (A, B) and polished sections (C, D, E, F, G, H) of samples aimed to observe the main foliation at the mesoscopic scale. All polished samples have been rotated to show approximatively the real dip of folition. Note that the orientation of the field exposures shown in A and B is the opposite to the orientation of samples shown in C, D, E, F, G and H. A. Exposure of fault rocks derived from Middle Triassic marls and limestones in site RC3 after digging. The foliation can be observed. B. Exposure in sampling sites RC6 where the foliation can be distinguished from color changes in the fault rocks. C. Polished section of sample RC5-A (well-cemented and mainly derived from limestones). Foliation is defined by orientation of long clasts and grains, some of them showing fractures perpendicular to foliation. D. Sample from site RC6-C, derived from Triassic sandstones and shales, where the foliation is defined by changes in color and grain size of different cataclastic bands. E. sample from site RC6-D, whose protolith corresponds to Middle Triassic or lowermost Jurassic dolostones, in which a large, fractured clast (without defined foliation) is surrounded by incipiently foliated, cemented cataclasite. F. Sample from site RC6-E derived from Triassic sandstones and shales and showing a banded structure defined by grain orientation, grain size and color. G. Sample from site RC6-G in which the foliation, defined by different colours of rock fragments, is folded according to an asymmetric fold consistent with reverse shear with top-to-the-North movement. H. Sample from site RC6-M showing clasts with their long axes parallel to the foliation plane, and cut by fractures that indicate an extension parallel to the dip direction of foliation. Incipient shear planes, more rectilinear and showing shallower dips, can also be distinguished.

Figure 3. Outcrop aspects of the fault rocks of the Rastraculos thrust (A, B) and polished sections (C, D, E, F, G, H) of samples aimed to observe the main foliation at the mesoscopic scale. All polished samples have been rotated to show approximatively the real dip of folition. Note that the orientation of the field exposures shown in A and B is the opposite to the orientation of samples shown in C, D, E, F, G and H. A. Exposure of fault rocks derived from Middle Triassic marls and limestones in site RC3 after digging. The foliation can be observed. B. Exposure in

sampling sites RC6 where the foliation can be distinguished from color changes in the fault rocks. C. Polished section of sample RC5-A (well-cemented and mainly derived from limestones). Foliation is defined by orientation of long clasts and grains, some of them showing fractures perpendicular to foliation. D. Sample from site RC6-C, derived from Triassic sandstones and shales, where the foliation is defined by changes in color and grain size of different cataclastic bands. E. sample from site RC6-D, whose protolith corresponds to Middle Triassic or lowermost Jurassic dolostones, in which a large, fractured clast (without defined foliation) is surrounded by incipiently foliated, cemented cataclasite. F. Sample from site RC6-E derived from Triassic sandstones and shales and showing a banded structure defined by grain orientation, grain size and color. G. Sample from site RC6-G in which the foliation, defined by different colours of rock fragments, is folded according to an asymmetric fold consistent with reverse shear with top-to-the-North movement. H. Sample from site RC6-M showing clasts with their long axes parallel to the foliation plane, and cut by fractures that indicate an extension parallel to the dip direction of foliation. Incipient shear planes, more rectilinear and showing shallower dips, can also be distinguished.

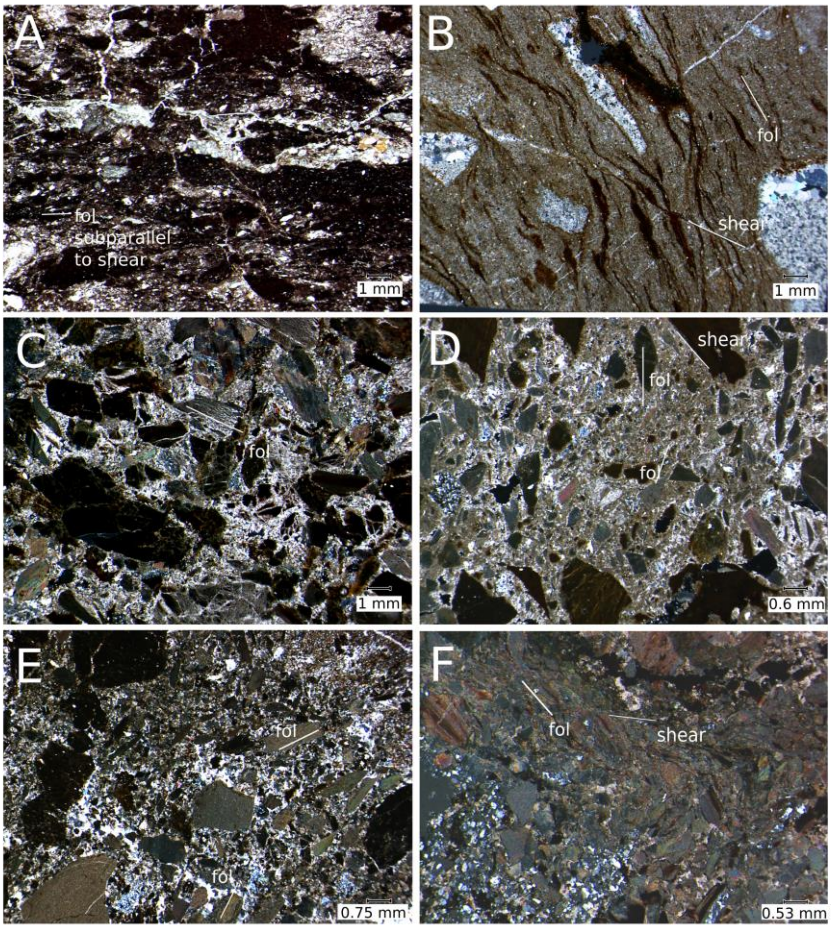

Figure 4. Photomicrographs of different fault rocks. A. Sample RC1-D15. Well-developed foliation in a fine-grained microbreccia showing abundant pelitic matrix, shaly fragments (practically opaque) and anisometric quartz grains oriented according to the dominant foliation. Pigmentary hematite is the responsible for the dark color of the rock in thin section. B. Sample RC2-E3. foliation and shear planes showing a reverse sense of movement in a fine-grained fault gouge with carbonate rock fragments. Both Foliation surfaces and shear planes are defined by concentration of iron oxides. North to the left of the image. C. Fault microbreccia of site RC3-B6, mainly consisting of carbonate fragments and cement. In this case, only a rough orientation of the long axis of grains defines the foliation planes. Some of the clasts are affected by calcite veins whose opening is parallel to the dip direction of the foliation planes. D. Calcareous microbreccia of site RC4-A14. Note the strongly anisometric grains to the right of the image. The dip of the foliation is subvertical but because of the irregularity of the surfaces the two dip senses (North and South are observed in detail). Only one shear, brittle surface (labelled in the upper part of the image) can be identified. North to the left of the image. E. Microbreccia of site RC5-C, in which a bimodal distribution of orientation of rock fragments can be observed. This distribution, suggest that the shallower dips of grains could be caused by shear deformation. F. Heterogeneous microbreccia of site RC6-H1 in which rough foliation and shear planes with reverse sense of movement can be defined. Foliation shows roughly sigmoidal shapes and shear planes, filled with iron oxides, show shallower or horizontal dips. North to the left of the image. See location of samples in figure 2.

Figure 4. Photomicrographs of different fault rocks. A. Sample RC1-D15. Well-developed foliation in a fine-grained microbreccia showing abundant pelitic matrix, shaly fragments (practically opaque) and anisometric quartz grains oriented according to the dominant foliation. Pigmentary hematite is the responsible for the dark color of the rock in thin section. B. Sample RC2-E3. foliation and shear planes showing a reverse sense of movement in a fine-grained fault gouge with carbonate rock fragments. Both Foliation surfaces and shear planes are defined by concentration of iron oxides. North to the left of the image. C. Fault microbreccia of site RC3-

B6, mainly consisting of carbonate fragments and cement. In this case, only a rough orientation of the long axis of grains defines the foliation planes. Some of the clasts are affected by calcite veins whose opening is parallel to the dip direction of the foliation planes. D. Calcareous microbreccia of site RC4-A14. Note the strongly anisometric grains to the right of the image. The dip of the foliation is subvertical but because of the irregularity of the surfaces the two dip senses (North and South are observed in detail). Only one shear, brittle surface (labelled in the upper part of the image) can be identified. North to the left of the image. E. Microbreccia of site RC5-C, in which a bimodal distribution of orientation of rock fragments can be observed. This distribution, suggest that the shallower dips of grains could be caused by shear deformation. F. Heterogeneous microbreccia of site RC6-H1 in which rough foliation and shear planes with reverse sense of movement can be defined. Foliation shows roughly sigmoidal shapes and shear planes, filled with iron oxides, show shallower or horizontal dips. North to the left of the image. See location of samples in figure 2.

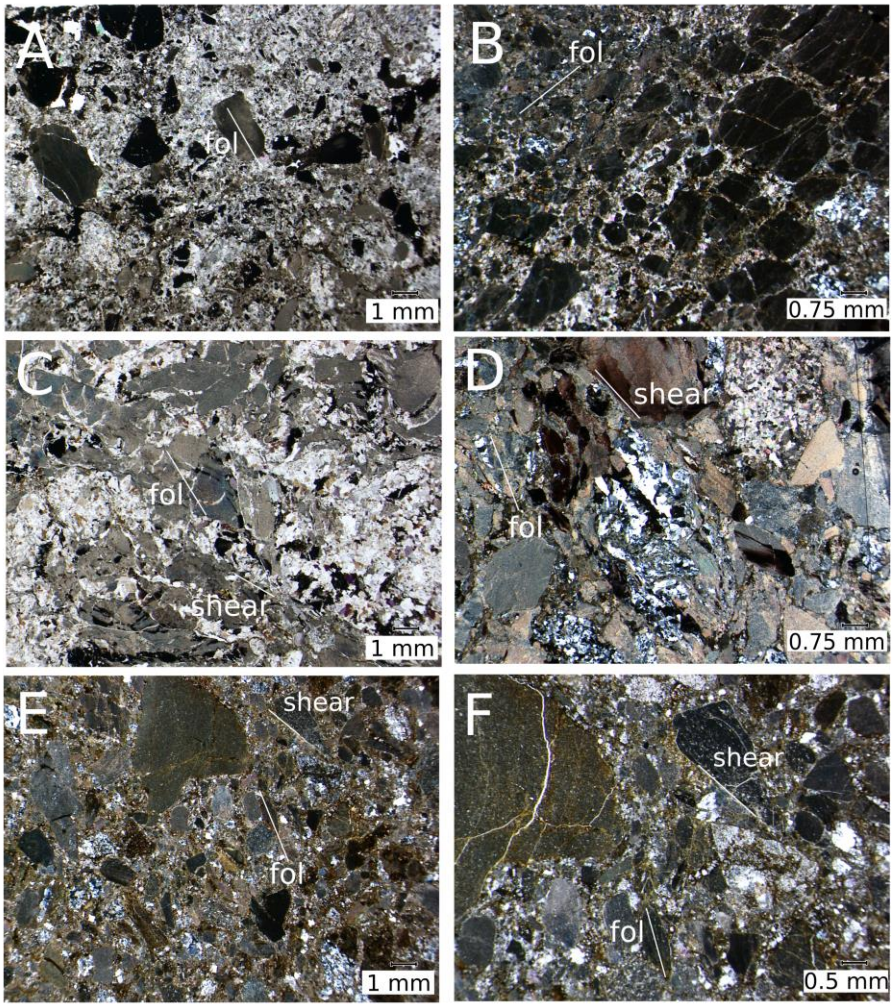

Figure 5. Photomicrographs of different fault rocks. A. Sample RC6-A17 in which foliation is only defined by the orientation of a few clasts of different size, North to the left of the image. B. Strongly oriented clasts due to fracturing and cataclasis in sample RC6-G. Although tension gashes show two maxima (parallel and perpendicular to the foliation), the thicker ones indicate an elongation parallel to the dip direction of the foliation. North to the right of the image. C. Well-developed foliation and shear planes in a calcareous breccia in sample RC6-N. Shear planes (dipping to the South) result in sigmoidal shapes of calcite grains. Opaque (probably ferromagnetic) grains fill both the shear surfaces and the spaces between grains. North to the left of the image. D. Well-developed foliation and shear planes in a calcareous breccia (sample RC6-O) in which sigmoidal shapes of calcite grains are consistent with shear along shallow-dippi ng shear surfaces. Both shear planes and foliation show precipitation of opaque minerals, although they are more abundant along shear planes. North to the left of the image. E. Heterogeneous microbreccia from sample RC5-A1. Foliation is defined by orientation of long axes of anisometric grains and occasional concentration of opaque minerals. Incipient shear planes, although not well defined, are sharper or can show thin crystalline fillings. North to the left of the image. F. Closer view of sample RC5-A1, with the same orientation. Average orientation of foliation and shear planes is shown. In this case, the different nature (that will be reflected in distinct magnetic properties) of both sets of planes (foliation defined by orientation of grains and shear planes by sharp boundaries and opaque fillings) can be seen.

Figure 5. Photomicrographs of different fault rocks. A. Sample RC6-A17 in which foliation is only defined by the orientation of a few clasts of different size, North to the left of the image. B. Strongly oriented clasts due to fracturing and cataclasis in sample RC6-G. Although tension gashes show two maxima (parallel and perpendicular to the foliation), the thicker ones indicate an elongation parallel to the dip direction of the foliation. North to the right of the image. C.

Well-developed foliation and shear planes in a calcareous breccia in sample RC6-N. Shear planes (dipping to the South) result in sigmoidal shapes of calcite grains. Opaque (probably ferromagnetic) grains fill both the shear surfaces and the spaces between grains. North to the left of the image. D. Well-developed foliation and shear planes in a calcareous breccia (sample RC6-O) in which sigmoidal shapes of calcite grains are consistent with shear along shallow-dipping shear surfaces. Both shear planes and foliation show precipitation of opaque minerals, although they are more abundant along shear planes. North to the left of the image. E. Heterogeneous microbreccia from sample RC5-A1. Foliation is defined by orientation of long axes of anisometric grains and occasional concentration of opaque minerals. Incipient shear planes, although not well defined, are sharper or can show thin crystalline fillings. North to the left of the image. F. Closer view of sample RC5-A1, with the same orientation. Average orientation of foliation and shear planes is shown. In this case, the different nature (that will be reflected in distinct magnetic properties) of both sets of planes (foliation defined by orientation of grains and shear planes by sharp boundaries and opaque fillings) can be seen.

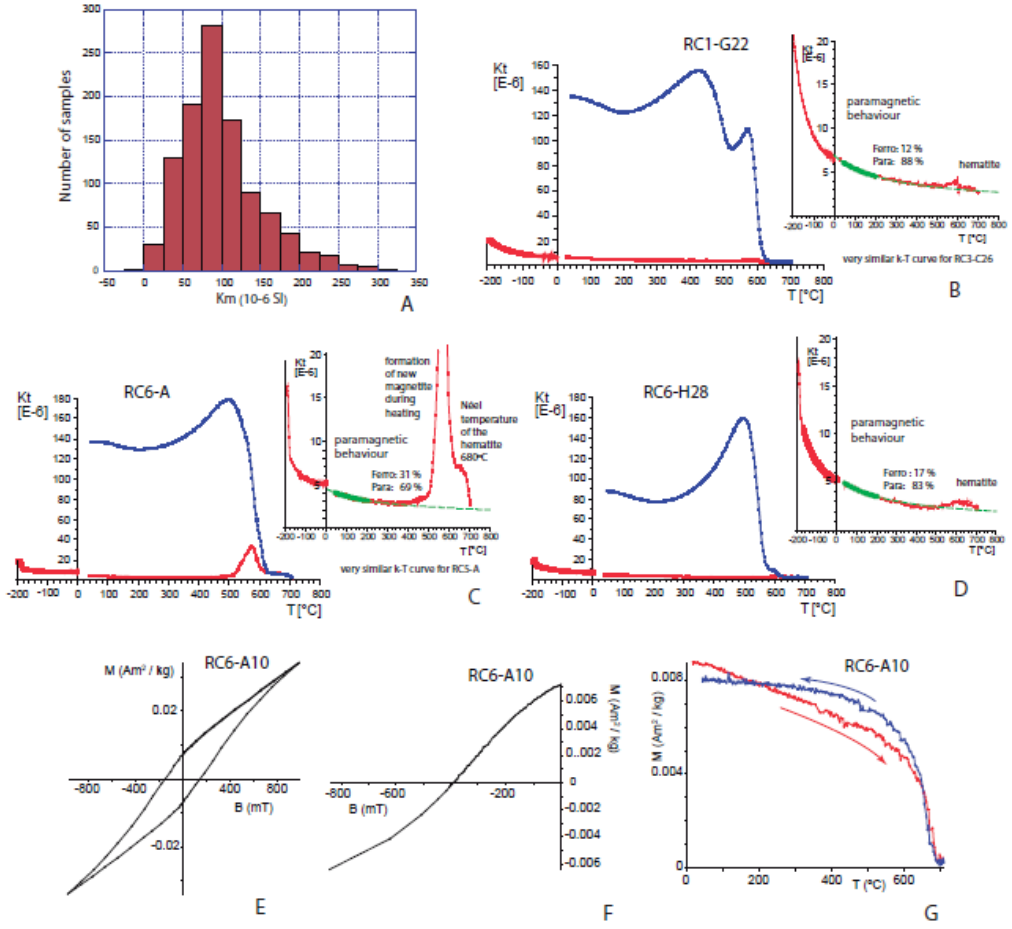

Figure 6. A. Histogram of the bulk susceptibility for the whole data. B, C, D. Temperature-susceptibility curves of different types of rocks found in the Rastraculos fault zone. B. Grey facies, sample RC1-G22. C. Red facies, sample RC6-A. D. Multi-colored facies, sample RC6-H28. E, F, G. Remanence rock magnetic experiments for sample RC6-A10. E. Hysteresis loop. F. Backfield curve. G. Magnetization thermomagnetic curve.

Figure 6. A. Histogram of the bulk susceptibility for the whole data. B, C, D. Temperature-susceptibility curves of different types of rocks found in the Rastraculos fault zone. B. Grey facies, sample RC1-G22. C. Red facies, sample RC6-A. D. Multi-colored facies, sample RC6-H28. E, F, G. Remanence rock magnetic experiments for sample RC6-A10. E. Hysteresis loop. F. Backfield curve. G. Magnetization thermomagnetic curve.

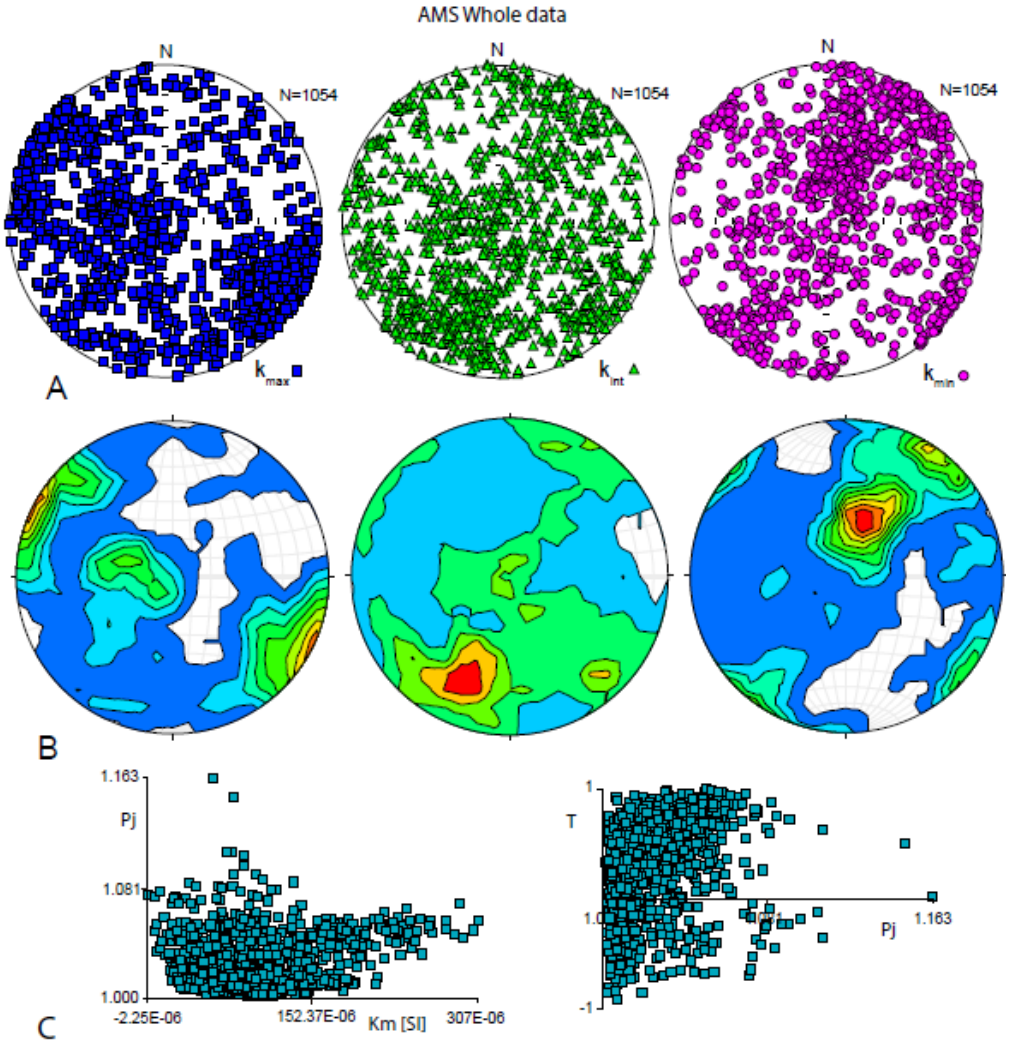

Figure 7. A. Directional analysis of AMS data: global stereoplots (k_{max}, k_{int}, k_{min}) for all specimens (lower hemisphere projection), B. Density dyagrams of AMS data (k_{max}, k_{int}, k_{min}) for all specimens (Kamb Contouring, contour interval = 2 sigma, significance level = 3; Stereonet software, Allmendinger et al. 2013; Cardozo & Allmendinger 2013), C. Km *versus* Pj, and Pj *versus* T graphs of whole data.

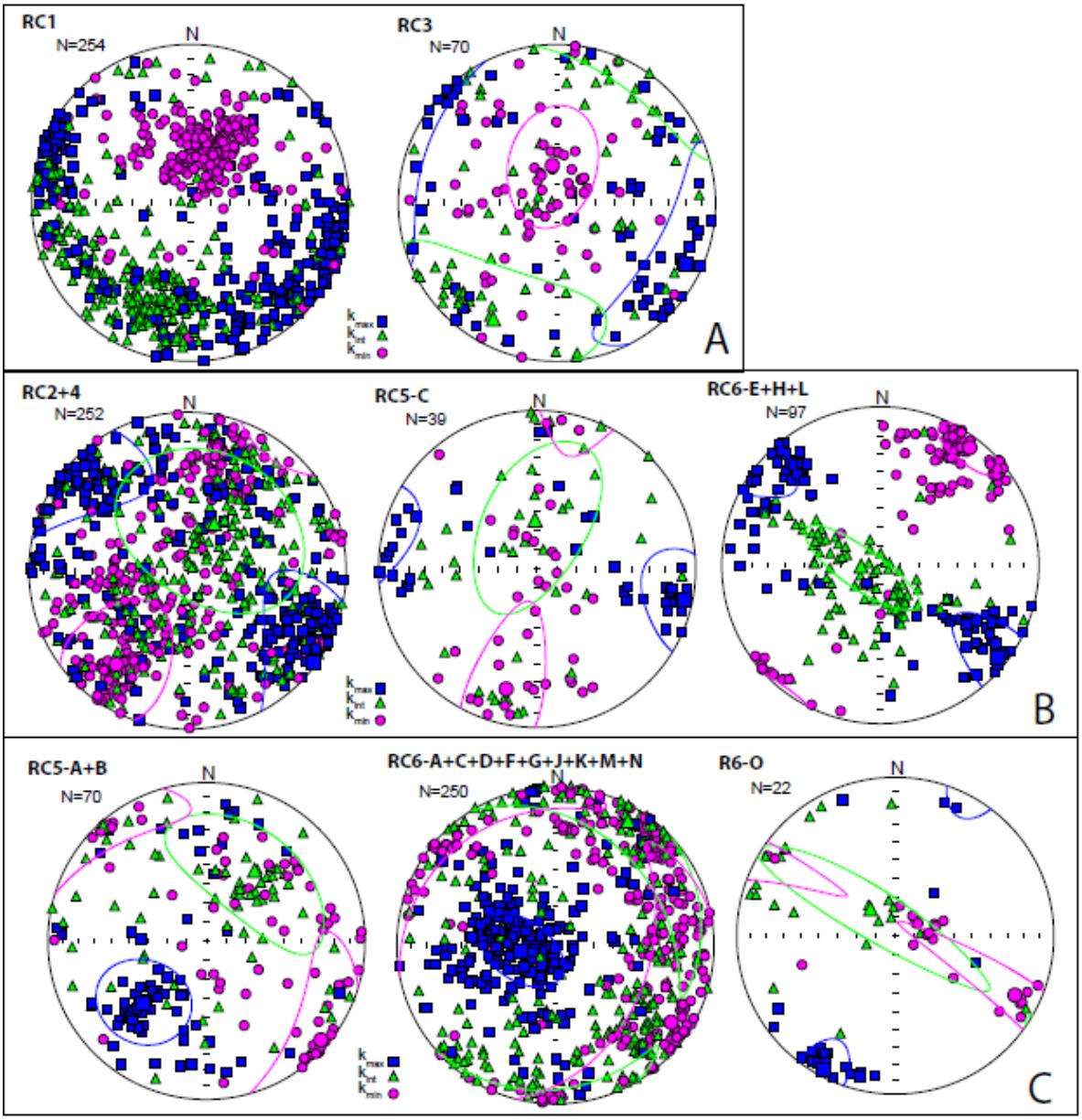

Figure 8. Directional data obtained from AMS analysis (lower hemisphere, equal area projection, mean vectors and confidence ellipses considering Jelinek statistics): partial results obtained in the different sampled sites, grouped according to the orientation distribution of the AMS axes. A. type 1 fabric, B. type 2 fabric, C, type 3 fabric (see text for explanation).

Figure 8. Directional data obtained from AMS analysis (lower hemisphere, equal area projection, mean vectors and confidence ellipses considering Jelinek statistics): partial results obtained in the different sampled sites, grouped according to the orientation distribution of the AMS axes. A. Type 1 fabric, B. Type 2 fabric, C. Type 3 fabric (see text for explanation).

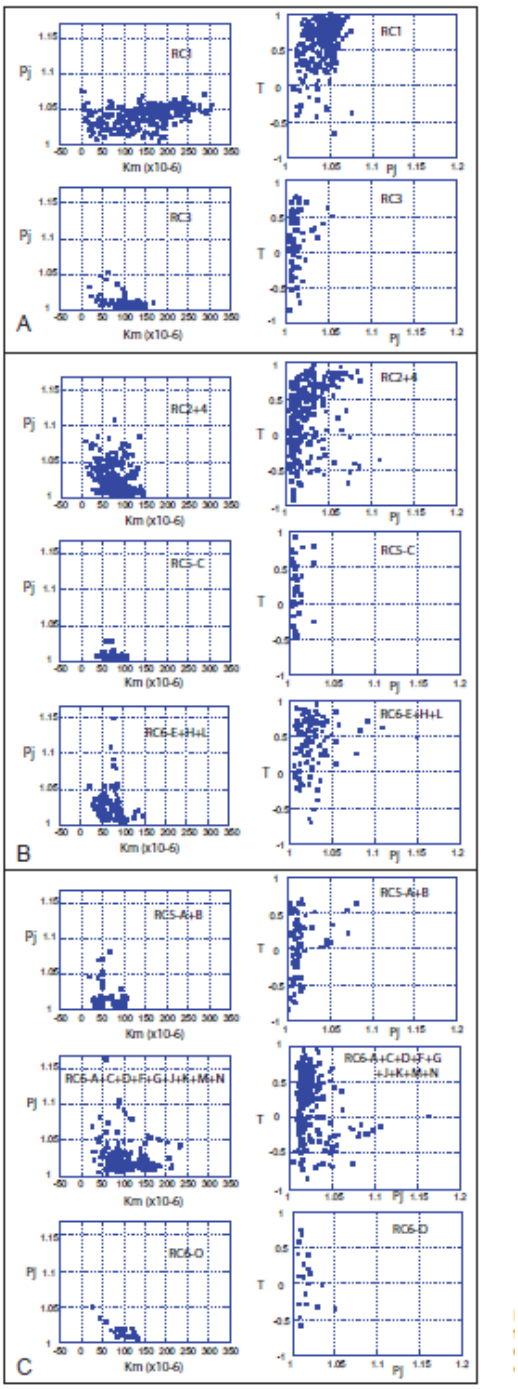

Figure 9. Km *versus* Pj, and Pj *versus* T graphs of all specimens from the different sites grouped according to the main patterns of the orientation of the AMS axes: A. Type 1 fabric, B. Type 2 fabric, C. Type 3 fabric (see text for explanation).

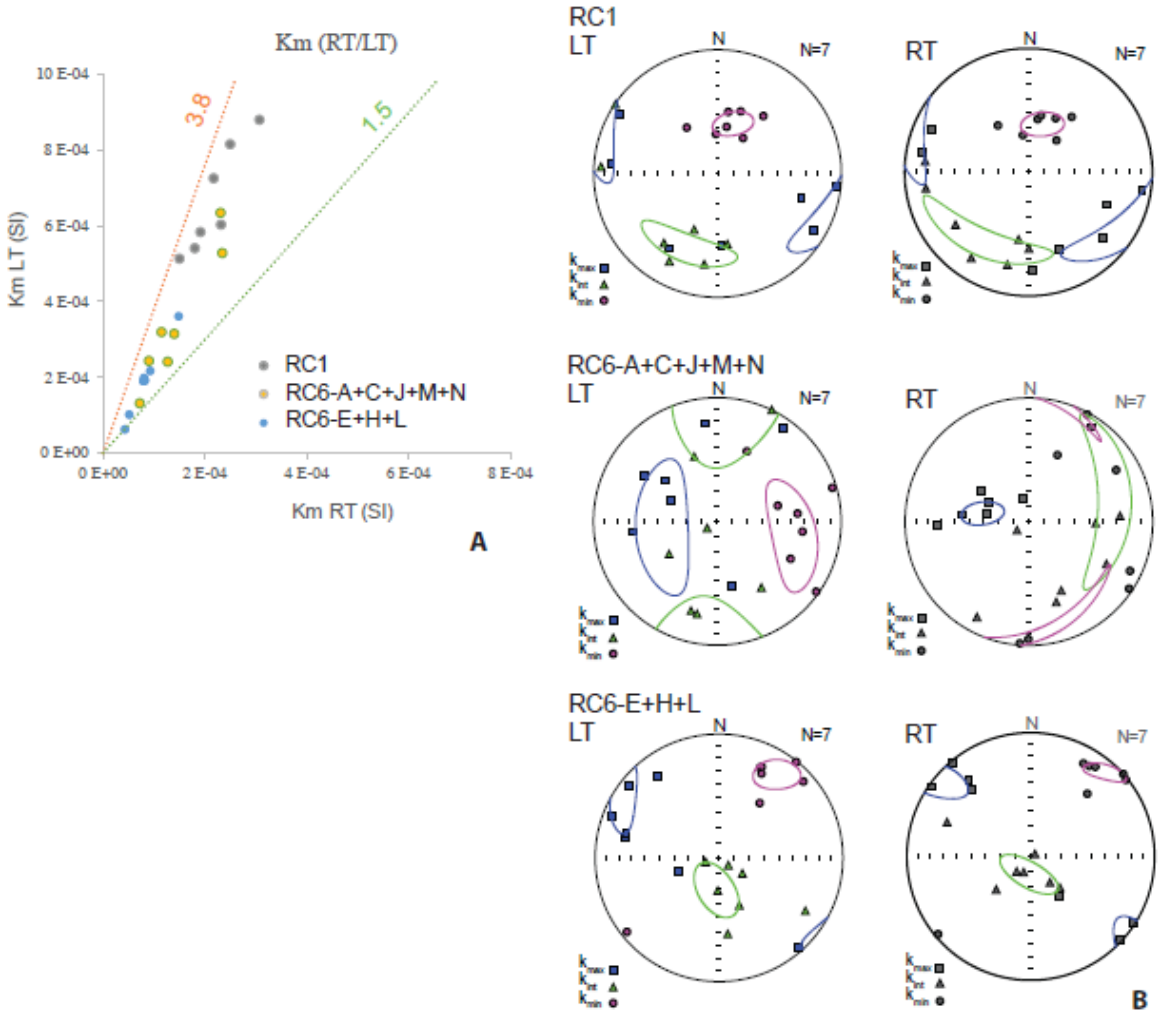

Figure 10. A. Diagram of magnetic susceptibility at room temperature (Km-RT) versus magnetic susceptibility at low temperature (Km-LT). B. Equal area projection of AMS results at room temperature and at low temperature.

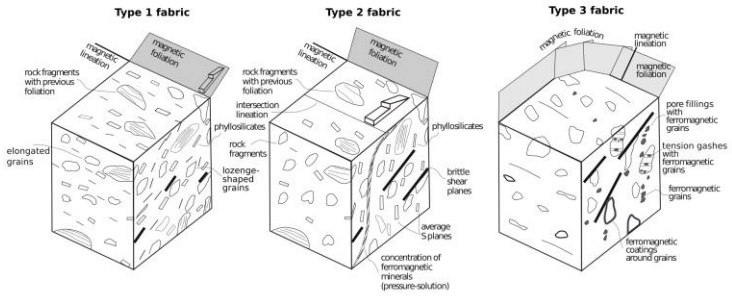

Figure 11. Interpretation of AMS results in the light of the relationships between petrofabric and magnetic fabrics. In types 1 and 2 fabrics, the magnetic lineation coincides with the intersection lineation between S and C′ planes and the magnetic foliation is parallel to the tectonic foliation. In Type 3 fabrics, the magnetic lineation is parallel to the projection of the transport direction onto the S planes of the S-C′ structures and the magnetic foliation is distributed within a girdle whose pole is the magnetic lineation.

Figure 11. Interpretation of AMS results in the light of the relationships between petrofabric and magnetic fabrics. In types 1 and 2 fabrics, the magnetic lineation coincides with the intersection lineation between S and C' planes and the magnetic foliation is parallel to the tectonic foliation. In Type 3 fabrics, the magnetic lineation is parallel to the projection of the transport direction onto the S planes of the S-C' structures and the magnetic foliation is distributed within a girdle whose pole is the magnetic lineation.

Table 1. Summary of the mean values of magnetic scalar data for each hand sample. n/N: number of specimens considered/analysed from each sample; Km: magnitude of the magnetic susceptibility (in 10^{-6} SI); Pj: anisotropy degree; T: shape parameter; St. dev.: standard deviation. LT: Lower Triassic, MT: Middle Triassic, LJ: Lower Jurassic, Ud.: Undefined.

Site	n/N	Color/Unit	Km ($\times10^{-6}$ SI)	St. dev. ($\times10^{-6}$ SI)	Pj	St. dev.	T	St. dev.
RC1-A	19/19	red/LT	92.4	68.1	1.038	0.009	0.613	0.383
RC1-B	46/47	red/LT	138.0	81.3	1.046	0.011	0.711	0.313
RC1-C	10/10	grey/LJ	125.0	25.8	1.042	0.009	0.164	0.202
RC1-D	21/21	red/LT	200.0	60.6	1.046	0.009	0.771	0.204
RC1-E	12/13	red/LT	104.0	58.3	1.046	0.007	0.620	0.217
RC1-F	7/7	multi-/Ud.	105.0	46.3	1.016	0.007	0.101	0.387
RC1-G	21/21	grey/LJ	150.0	35.6	1.044	0.013	0.402	0.277
RC1-H	10/10	multi-/Ud.	132.0	45.3	1.015	0.008	0.322	0.345
RC1-I	13/13	grey/LJ	171.0	54.8	1.028	0.015	0.516	0.383
RC1-J	9/9	grey/LJ	112.0	46.2	1.049	0.006	0.582	0.186
RC1-K	30/30	multi-/Ud.	165.0	29.3	1.048	0.006	0.562	0.200
RC1-L	22/22	red/LT	215.0	53.8	1.049	0.012	0.824	0.171
RC1-M	15/15	yellow/MT	102.0	59.2	1.022	0.004	0.673	0.224
RC1-N	19/19	yellow/MT	63.3	39.8	1.028	0.013	0.536	0.250
RC1	**254/256**		**140.0**	**69.3**	**1.040**	**0.014**	**0.587**	**0.319**
RC2-A	20/20	grey/LJ	62.1	16.3	1.023	0.011	0.362	0.447
RC2-B	11/11	grey/LJ	66.5	8.1	1.026	0.007	0.676	0.255
RC2-C	29/29	grey/LJ	73.1	20.8	1.023	0.012	0.384	0.288
RC2-D	17/17	grey/LJ	42.1	15.6	1.038	0.016	0.358	0.406
RC2-E	14/14	grey/LJ	87.4	16.5	1.058	0.010	0.778	0.098
RC2-F	14/14	grey/LJ	52.3	23.5	1.054	0.015	0.622	0.305
RC2-G	8/8	grey/LJ	57.0	27.3	1.040	0.011	0.486	0.311
RC2	**113/113**		**63.9**	**22.8**	**1.035**	**0.018**	**0.490**	**0.367**
RC3-A	34/34	yellow/MT	100.0	36.6	1.010	0.008	0.111	0.373
RC3-B	11/11	grey/LJ	90.0	29.5	1.011	0.008	0.048	0.486
RC3-C	25/25	grey/LJ	78.4	30.5	1.016	0.012	0.266	0.350
RC3	**70/70**		**90.8**	**34.5**	**1.013**	**0.010**	**0.157**	**0.388**
RC4-A	49/49	yellow/MT	84.5	24.4	1.015	0.018	0.049	0.376
RC4-B	13/13	yellow/MT	95.4	30.9	1.012	0.009	0.145	0.417
RC4-C	34/34	yellow/MT	99.1	21.8	1.013	0.017	0.093	0.475
RC4-D	17/17	yellow/MT	106.0	24.0	1.009	0.003	-0.096	0.359
RC4-E	17/17	yellow/MT	92.6	32.5	1.034	0.025	-0.166	0.321
RC4-F	9/9	yellow/MT	97.7	36.9	1.018	0.023	0.165	0.456
RC4	**139/139**		**93.6**	**27.0**	**1.016**	**0.018**	**0.032**	**0.409**
RC5-A	26/26	yellow/MT	39.0	8.7	1.016	0.014	0.012	0.443
RC5-B	44/44	yellow/MT	84.8	17.8	1.017	0.018	0.044	0.397
RC5-C	39/39	yellow/MT	74.4	20.1	1.009	0.006	0.257	0.366
RC5	**109/109**		**70.2**	**24.8**	**1.014**	**0.014**	**0.113**	**0.409**
RC6-A	23/23	red/LT	97.7	40.1	1.028	0.022	-0.004	0.459
RC6-C	31/31	multi-/LT	158.0	39.0	1.032	0.023	0.008	0.443
RC6-D	30/30	yellow/MT-LJ	79.4	21.6	1.039	0.037	0.042	0.414
RC6-E	37/37	multi-/LT	77.7	13.7	1.040	0.029	0.493	0.327
RC6-F	25/25	red/LT	99.2	35.3	1.018	0.006	0.408	0.298
RC6-G	33/33	yellow/MT	83.7	11.7	1.015	0.004	0.461	0.274
RC6-H	28/28	multi-/Ud.	88.0	26.8	1.013	0.006	0.377	0.348
RC6-J	32/32	multi-/Ud.	120.0	46.1	1.020	0.010	0.295	0.378
RC6-K	16/16	yellow/MT	80.2	31.2	1.024	0.009	0.388	0.314

RC6-L	32/32	yellow/MT	52.2	14.7	1.029	0.009	0.267	0.384
RC6-M	42/42	grey/LJ	98.1	13.1	1.018	0.011	0.214	0.382
RC6-N	18/18	grey-red/Ud.	117.0	37.5	1.026	0.010	0.483	0.283
RC6-O	22/22	grey/LJ	95.1	28.6	1.016	0.010	0.052	0.398
RC6	**369/369**		**95.5**	**37.9**	**1.025**	**0.020**	**0.267**	**0.403**

Table 2. Summary of magnetic directional data (mean orientations for each hand sample). k_{max}, k_{int}, k_{min}: mean orientations (Dec/Inc: declination/inclination) considering the Jelinek statistic (Jelinek 1978); Conf. angles: confidence angles.

Site	Latitude/Longitude	k_{max} Dec/Inc	Conf. angles	k_{int} Dec/Inc	Conf. angles	k_{min} Dec/Inc	Conf. angles
RC1-A		111/38	64/7	218/20	64/12	329/46	16/8
RC1-B		127/14	69/9	224/28	69/6	013/58	10/6
RC1-C		277/15	7/3	176/36	9/4	026/50	7/3
RC1-D		122/14	62/5	216/14	62/6	349/69	7/4
RC1-E		117/07	27/10	210/29	27/5	015/60	13/3
RC1-F		185/11	36/13	282/32	33/21	079/55	23/19
RC1-G		292/03	22/9	201/29	22/9	027/61	10/8
RC1-H		057/18	31/16	167/48	32/28	313/37	30/16
RC1-I		166/18	18/16	265/26	41/10	045/57	40/17
RC1-J		119/12	18/5	215/28	17/4	009/59	8/3
RC1-K		119/02	28/9	211/49	28/13	027/41	15/6
RC1-L		192/24	59/8	285/7	59/8	031/65	10/6
RC1-M		124/09	51/12	223/42	51/9	024/46	13/9
RC1-N		134/12	41/16	229/22	41/18	017/64	19/15
RC1	N42°4'56.24"/ W2°49'27.66"	**120/09**	**53/14**	**215/29**	**53/14**	**015/59**	**16/12**
RC2-A		304/14	63/16	041/24	63/14	186/61	22/18
RC2-B		152/21	77/10	050/29	77/9	272/53	10/9
RC2-C		127/21	22/9	025/30	25/18	248/52	22/9
RC2-D		304/01	11/6	036/70	14/9	214/20	14/7
RC2-E		135/49	15/8	264/28	14/8	010/26	12/7
RC2-F		310/12	40/6	080/71	40/5	217/14	7/5
RC2-G		305/21	28/9	121/69	30/9	214/01	16/7
RC2	N42°4'54.58"/ W2°49'42.13"	**125/07**	**28/11**	**023/59**	**30/23**	**219/30**	**26/12**
RC3-A		101/32	34/21	225/41	76/30	348/31	76/26
RC3-B		133/04	11/6	224/07	54/7	014/82	54/6
RC3-C		127/05	62/17	218/16	62/9	021/74	18/7
RC3	N42°4'53.54"/ W2°49'40"	**115/11**	**49/22**	**208/16**	**49/31**	**353/71**	**33/22**
RC4-A		214/67	85/41	119/02	85/31	028/23	48/34
RC4-B		325/05	52/22	055/03	66/51	174/84	66/25
RC4-C		099/05	33/11	196/53	34/25	006/36	26/11
RC4-D		113/15	17/6	258/72	21/13	020/10	18/5
RC4-E		341/39	20/9	157/50	41/20	249/02	41/6
RC4-F		238/07	16/1	024/82	43/10	147/05	42/1
RC4	N42°4'53.54"/ W2°49'40"	**300/18**	**71/59**	**145/70**	**74/65**	**032/08**	**74/61**
RC5-A		213/47	71/42	337/27	73/65	084/30	69/46
RC5-B		227/41	16/7	045/49	16/12	136/01	13/6
RC5-C		102/06	29/18	357/66	050/26	194/23	50/16

RC5	N42°5'2.38"/ W2°50'18.3"	**235/42**	**41/33**	**057/48**	**65/40**	**326/01**	**66/30**
RC6-A		300/65	12/5	107/25	56/11	199/05	56/5
RC6-C		278/53	7/3	110/36	57/7	015/06	57/3
RC6-D		223/79	10/4	036/11	29/7	126/01	29/5
RC6-E		125/26	14/6	285/63	14/5	031/08	7/4
RC6-F		201/67	29/7	344/18	30/21	078/13	23/7
RC6-G		294/68	10/5	135/21	10/5	042/07	7/4
RC6-H		295/01	27/13	203/60	28/18	026/29	19/14
RC6-J		255/78	24/9	024/08	30/18	116/09	27/7
RC6-K		291/66	43/11	041/09	43/7	135/22	11/8
RC6-L		319/19	14/5	150/71	14/9	050/03	9/4
RC6-M		247/59	30/12	110/23	36/21	012/18	33/13
RC6-N		158/81	42/11	039/04	42/19	308/07	20/10
RC6-O		208/05	21/9	314/72	75/13	116/17	75/8
RC6	N42°5'2.38"/ W2°50'18.3"	**267/73**	**35/16**	**131/13**	**47/35**	**038/12**	**47/16**